Available online at www.sciencedirect.com
ScienceDirect
Comput. Methods Appl. Mech. Engrg. 405 (2023) 115865
Computer methods in applied mechanics and engineering
www.elsevier.com/locate/cma

Energy–time optimal path planning in dynamic flows: Theory and schemes

Manan M. Doshi[1], Manmeet S. Bhabra[1], Pierre F.J. Lermusiaux[*]

Department of Mechanical Engineering, Massachusetts Institute of Technology, 77 Mass. Ave., Cambridge, MA 02139, United States of America

Received 1 May 2022; received in revised form 17 December 2022; accepted 19 December 2022
Available online xxxx

Abstract

We obtain, solve, and verify fundamental differential equations for energy–time path planning in dynamic flows. The equations govern the energy–time reachable sets, optimal paths, and optimal controls for autonomous vehicles navigating to any destination in known dynamic environments, minimizing both energy usage and travel time. Based on Hamilton–Jacobi theory for reachability and the level set method, the resulting methodology computes the Pareto optimal solutions to the multi-objective path planning problem, numerically solving the exact equations governing the evolution of reachability fronts and optimal paths in the augmented energy and physical-space domain. Our approach is applicable to path planning in various dynamic flow environments and energy types. We first validate the methodology through a benchmark case of crossing a steady jet for which we compare our results to semi-analytical optimal energy–time solutions. We then consider unsteady flow environments and solve for energy–time optimal missions in a quasi-geostrophic double-gyre flow field. Results show that our theory and schemes can provide all the energy–time optimal solutions and that these solutions can be strongly influenced by unsteady flow conditions.

Keywords: Path planning; Time-optimal; Energy-optimal; Multi-objective optimization; Hamilton–Jacobi; Reachability

1. Introduction

The growth of autonomous vehicles has been staggering in the last decade. Self driving cars, autonomous drones, and underwater vehicles have all seen a surge of interest [e.g. 1–6]. Central to the effective operation of all autonomous vehicles is efficient and accurate motion control which falls under the purview of path planning. Path planning, in the most general sense, corresponds to a set of rules to be provided to an autonomous robot for moving from one configuration to another in some optimal fashion [7]. The metric for optimality depends on the application and specific objectives of the user. It includes optimizing for travel time, energy employed, vehicle safety, or quality of collected data to name a few [8,9]. Increasingly, the requirements for vehicles to operate autonomously for longer duration in harsh conditions [10] and the need to sustain the health of our planet [11,12] have resulted in the ever-increasing importance of energy optimization. In particular, one can optimize vehicles and propulsion

* Corresponding author.
E-mail addresses: mdoshi@mit.edu (M.M. Doshi), mbhabra@mit.edu (M.S. Bhabra), pierrel@mit.edu (P.F.J. Lermusiaux).
[1] Equal contribution.

https://doi.org/10.1016/j.cma.2022.115865
0045-7825/

systems, or better use the environment to minimize energy consumption. There are indeed many applications where the environment can play a significant role in the sustainable navigation of marine, land, and air vehicles [13]. The novel focus of this work is on exact equations and computational methods for the joint energy–time optimal path planning of autonomous vehicles navigating in known strong and dynamic environments. The theory and schemes are verified in the ocean context but the results are applicable to other environments.

The energy requirements of marine vehicles are diverse. In addition to the power required for the propulsion system itself, power is also needed for non-propulsive purposes – what is known as the "hotel" load – for components such as the sonar system for mapping and systems for data transmission and reception [14]. When navigating from a start point to the desired destination, energy efficiency ultimately comes from two major sources: (1) The vehicle itself such as new designs, propulsion systems, and power systems, or (2) The controls such as headings and speeds that optimize energy expenditure. The former includes novel vehicle designs based on hydrodynamic characteristics [15]. In particular, the TETHYS vehicle [16] achieves energy efficiency by minimizing drag and maximizing propeller efficiency. New power systems include Solar-powered Autonomous Underwater Vehicles (SAUV) [17], several of which enable recharge of the onboard energy system when the vehicle returns to the surface [18–21]. Improved power sources with higher energy and power density, lower cost, and longer life [22,23] also include new battery cells, semi-fuel cells, and even flywheel batteries [24–27].

Our focus here is the second approach for energy–time efficiency: predict controls and paths that optimize both energy and time. Path planning for autonomous vehicles has been extensively studied, especially for static environments [28,29]. The ocean environment is however a harsh and highly dynamic system with considerable variability in time and space. Strong currents and waves have a significant influence. The speeds of currents are often either comparable to that of vehicles, such as for Autonomous Underwater Vehicles (AUVs) [30], or much larger than vehicle speeds, such as for gliders [7,31]. It is then imperative to account for the dynamic nature of ocean currents and their effect on the resulting vehicle path. Similar statements can be made for birds, drones, or planes in strong winds and gusts [32,33]. In general, vehicles can save significant energy by leveraging the external flow field such that, when and where flows are favorable, the thrust can be reduced and energy can be saved. Due to the spatial complexity and variability of currents and winds, and to the corresponding undetermined optimal control equations, it is however not obvious to predict which regions are reachable, which paths to take, and when/where to slow down, so as to reach the destination in minimum time and energy. The critical challenges are to predict the flows in time and space, and to predict the reachable sets [34] (set of all states reachable from a given starting state, as defined formally in Section 3.1) and optimal paths for the joint energy-and-time control optimization in these flows. If currents or winds are assumed known, the central questions remaining are: what are the equations that govern the energy–time optimal control and path solutions, and what are efficient numerical schemes for solving these equations?

In this work, we develop fundamental differential equations that govern the reachable locations and the power and headings that optimize the energy usage and travel time of vehicles navigating in deterministic dynamic flows. Given a start location, final destinations, initial energy, and power–speed relations, our methodology then predicts the corresponding optimal paths. The differential equations we obtain use Hamilton–Jacobi theory and govern reachable sets and globally optimal paths for energy–time path planning in dynamic environments. Results drastically generalize the time optimal results [35] through state augmentation and multi-dimensional differential optimization; as we will see, partial derivatives will now be taken with respect to both energy and physical space. The methodology solves for the family of all solutions that lie on the Pareto front of the multi-objective optimization problem with energy and time as cost functions. Users can then select any optimal solution(s) that they prefer based on how highly they value minimizing energy usage or travel time, or on some weighted combination of the two.

In what follows, we first briefly review existing methods for energy-efficient path planning. In Section 2, we present the general problem statement and introduce key notation. Section 3 develops the theory and equations for energy–time optimal path planning in dynamic flows. Numerical schemes to solve these equations are provided in Appendix A. In Section 4, applications and numerical results for path planning in highly dynamic environments are described, followed by the conclusions and discussions on future work in Section 5.

1.1. Approximate energy optimal path planning in dynamic flows

Several methods have been proposed for energy-efficient path planning. For methods using graph search schemes, the state space is discretized into a grid with weighted nodes. The optimal path from the start to the target in this

discrete space is then turned into a graph search problem which can be solved using a depth-first search, breadth-first search, Dijkstra's method, or the A* algorithm [36]. Graph search methods have been applied extensively for autonomous path planning [37], some incorporating energy efficiency. For instance, Garau et al. [38] build upon Carroll et al. [37] to determine optimal paths (in terms of energy cost) in ocean environments consisting of eddies and currents. Kularatne et al. [39] consider graph search based methods for generating time and energy optimal paths while also considering kinematic constraints on vehicle operation. Huynh et al. [40] use nonlinear robust Model Predictive Control where optimal paths are found using an A*-like algorithm. Finally, Koay and Chitre [41] studied the effectiveness of current-aware energy-efficient paths for AUVs using an A* algorithm.

Rapidly Explore Random Trees (RRTs) algorithms use random sampling to explore a space and have been employed for energy-efficient path planning. For example, in Rao and Williams [42], RRTs find feasible paths for gliders and subsequently use an A* search to identify a path from this collection that minimizes an energy-based metric.

Evolutionary algorithms for path planning have also been developed and, within this class, the genetic algorithm (GA) and particle swarm optimization (PSO) algorithm are two of the most popular [43]. Alvarez et al. [44] use a genetic algorithm approach on a grid to find possible minimum energy cost paths in spatially and temporally variable ocean environments. Cao et al. [45] consider a framework for optimal path planning for underwater gliders in 3D space that uses a modified 3D Dubins curve to obtain candidate paths and then uses a genetic algorithm to generate optimal trajectories that minimize energy consumption. Huang et al. [46] uses receding horizon control along with particle swarm optimization to generate trajectories that are energy optimal for solar-powered vehicles for the purpose of target tracking. An issue for all of these GA and PSO schemes is the lack of theoretical guarantees for global optima.

Several algorithms also search for optimal continuous paths by formulating the path planning problem as a nonlinear optimization problem. Kruger et al. [47] compute paths by solving an optimization problem in which energy usage is added to the search space, thus allowing for the vehicle thrust to be modified to minimize energy expenditure. Witt and Dunbabin [48] then extend these results by optimizing continuous paths in a search space that includes time, obstacles, traversability, propulsion energy, and speed.

Stochastic optimization methods based on partial differential equations (PDEs) have been developed for energy optimal path planning [9,49]. The vehicle speed is then treated as a dynamic random variable, rendering the Hamilton–Jacobi PDE stochastic. The Dynamically Orthogonal (DO) equations are used to optimally reduce the stochastic PDE and compute minimum energy paths among the sampled distribution of time optimal paths.

All the above methods are useful, especially for static environments or for problems where approximate solutions are sufficient. In strong dynamic flows, however, most of these methods cannot provide the exact optimal energy–time solutions efficiently. In particular, for time-optimality, graph search methods have been shown to be less efficient than solving the exact Hamilton–Jacobi (HJ) equations [50].

2. Problem statement

Energy–time optimal path planning is a multi-objective optimization problem with competing objectives: reach the destination (i) as quickly as possible and (ii) using the minimum energy possible. These objectives are often competing since the vehicle can typically reach the destination faster if it uses more energy.

In general, non-trivial multi-objective optimization problems do not have a unique global solution that optimally satisfies each objective [51]. In these cases, a possibly infinite set of solutions exists, where each candidate solution is said to be Pareto optimal [52]. A Pareto optimal solution is one that cannot be improved upon in any objective without degrading the performance of at least one other objective [53]. The set of Pareto solutions is referred to as the *Pareto front*. In the case of energy–time optimal path planning, where the two objectives are minimizing the arrival time and the vehicle energy use, any Pareto optimal solution will correspond to one where the destination cannot be reached any faster while arriving with the same amount of energy or, where the destination cannot be reached using less energy given the same amount of time, see Fig. 1(a) –1(b).

In this work, the goal is to solve for the whole Pareto front, deriving and using the exact differential equations for optimal energy–time reachability. Our goal thus includes three classes of common problems:

a. Time optimal path planning with an energy constraint.
b. Energy optimal path planning with a time constraint.
c. Energy–time optimal path planning, or any arbitrary solution(s) on the energy–time Pareto front.

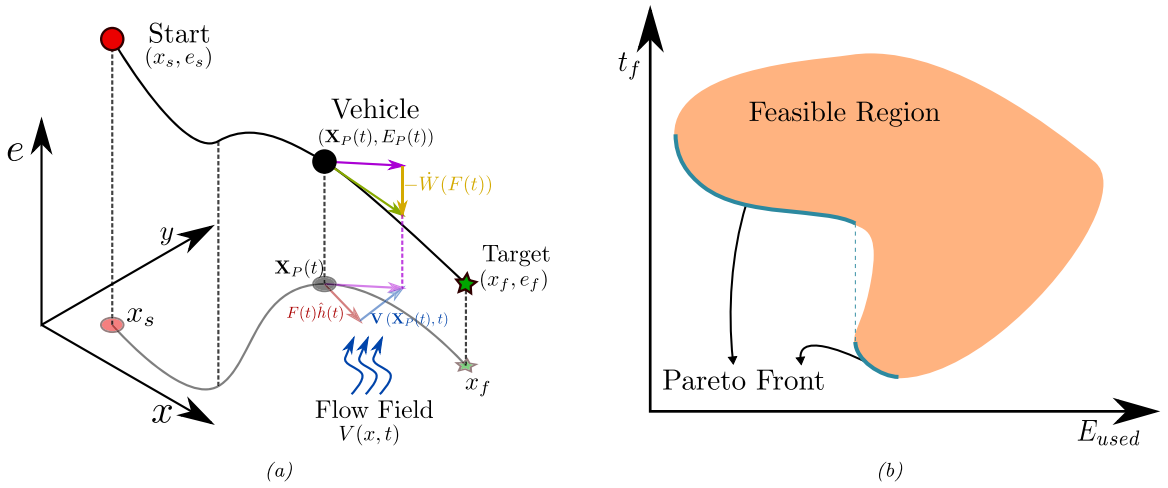

Fig. 1. Problem Statement: Energy–time optimal path planning. (a) Schematic describing the vehicle dynamics in the augmented energy and physical-space domain. In physical space (x, y, z; z not shown), the vehicle travels from a start point ($\boldsymbol{x}_s$: •) to a target final point ($\boldsymbol{x}_f$: ★) and is forced by an external flow field ($\boldsymbol{V}$: →). The net physical-space velocity of the vehicle ($\frac{\mathrm{d}\boldsymbol{X}_p}{\mathrm{d}t}$: →) is the sum of this external flow velocity ($\boldsymbol{V}$: →) and the nominal propulsion velocity of the vehicle ($F(t)\,\hat{\boldsymbol{h}}(t)$: →). As the vehicle travels, it also loses energy. If we consider the vehicle in the augmented state space, i.e. the joint energy and physical-space domain (x, y, z, e; z not shown), its velocity in the energy dimension is the power loss or rate of energy lost due to propulsion ($-\dot{W}$: →). The net generalized velocity of the vehicle in the augmented state space (→) is the sum of these velocities: the net physical-space and power-loss velocities. (b) Pareto Front in the time and energy domain. In multi-objective optimization, the performance of Pareto solutions cannot be improved without worsening the performance for other objectives. The above sketch shows the performance of various feasible solutions on the two objectives we wish to minimize — the time to reach the destination (t_f) and the Energy used (E_{used}). The set of feasible solutions forms the feasible region. The Pareto front or all optimal solutions are marked in blue. (For interpretation of the references to color in this figure legend, the reader is referred to the web version of this article.)

2.1. Problem parameters

Consider a vehicle tasked with navigating in a physical domain $\Omega \subseteq \mathbb{R}^d$ from a start point $\boldsymbol{x}_s$ to a specified target point $\boldsymbol{x}_f$, starting at initial time $t_s = 0$ with an initial energy e_s. The position and energy available of the vehicle at time t are denoted by $\boldsymbol{X_p}(t)$ and $E_p(t)$, respectively, where the energy available should remain positive $E_p(t) > 0 \;\; \forall t \in [t_s, t_f]$. These set of conditions and constraints can be written as

$$\boldsymbol{X_p}(0) = \boldsymbol{x}_s \tag{1a}$$
$$E_p(0) = e_s \tag{1b}$$
$$\boldsymbol{X_p}(t_f) = \boldsymbol{x}_f \tag{1c}$$
$$E_p(t) > 0 \;\; \forall t \in [t_s, t_f]\,. \tag{1d}$$

Along its path, the vehicle has two propulsion controls that it uses to solve the optimal planning problem at hand: (i) its time-dependent nominal speed $F(t) \in [0, F_{\max}]$, $F_{\max} \in \mathbb{R}$, and (ii) its heading direction, which may be time-dependent, and represented by a unit vector, $\{\hat{\boldsymbol{h}}(t) \in \mathbb{R}^d \;:\; \|\hat{\boldsymbol{h}}(t)\|_2 = 1\}$. For convenience, we summarize the main problem parameters in Table 1.

The vehicle operates in a large-scale environment with an assumed known deterministic background dynamic flow field $\boldsymbol{V}(\boldsymbol{x}, t) : \Omega \times (0, \infty) \to \mathbb{R}^d$. In practice, this known flow field could be provided by a model or data-driven forecast [5]. The spatial dimensions of the vehicle, $\mathcal{O}$ (m), are in general much smaller than the spatial scales, $\mathcal{O}$ ($\gg$ 100 m), of both the background flow and distance to travel. The control of the local vehicle motions, handled by a local controller, is thus not considered here. In this work, the vehicle is modeled as a point particle whose motion through the physical space is governed by the relative motion due to its thrust and advection from the large-scale background flow. While navigating, the vehicle uses energy for thrust and to power its various components needed for operation. We assume that the latter is on average relatively constant or negligible compared to the former. We

Table 1
Summary of main problem parameters.

$\boldsymbol{x}, e, t$	Physical-space, energy and time coordinates	$\boldsymbol{X_p}(t)$	Vehicle position at time t
$\boldsymbol{x}_s$	Start point	$E_p(t)$	Vehicle energy at time t
$\boldsymbol{x}_f$	Target point	$F(t)$	Vehicle nominal speed at time t
e_s	Initial vehicle energy at start point	F_{max}	Maximum vehicle nominal speed
e_f	Final vehicle energy at target point	$\hat{\boldsymbol{h}}(t)$	Vehicle heading at time t
t_s	Start time	$\boldsymbol{V}(\boldsymbol{x}, t)$	Spatio-temporal velocity field
t_f	Final time	$\dot{W}(F)$	Energy loss rate as a function of vehicle speed
k, n	Parameters of the power–energy law		

focus here on the power consumed for thrust generation, and assume it is mostly a function of the nominal vehicle speed: $\dot{W} = \dot{W}(F(t))$. Combining the evolution of the vehicle position with the energy evolution governed by the first law of thermodynamics, the full dynamics of the vehicle's state is given by the ordinary differential equations (ODEs):

$$\frac{\mathrm{d}\boldsymbol{X_p}}{\mathrm{d}t} = \boldsymbol{V}\left(\boldsymbol{X_p}(t), t\right) + F(t)\,\hat{\boldsymbol{h}}(t)\,, \tag{2a}$$

$$\frac{\mathrm{d}E_p}{\mathrm{d}t} = -\,\dot{W}(F(t)). \tag{2b}$$

The vehicle and environmental dynamics are schematized in Fig. 1(a). In Eq. (2b), there exist several models for the thrust power function including $\dot{W} \propto F(t)$ for constant drag-force, $\dot{W} \propto F(t)^2$ for linear drag, $\dot{W} \propto F(t)^3$ for quadratic drag, or, for more accurate models, a combination thereof [9,54–56]. In our derivations, we consider the generic monomial $\dot{W}(F(t)) = k \cdot F(t)^n$ where n is a positive integer and $k \in \mathbb{R}^+$ is independent of F and commonly a constant of proportionality. In the examples, we assume only a quadratic drag, and thus model the power consumption as $\dot{W}(F(t)) = k \cdot F(t)^3$. We note that the application determines the complexity needed for the power usage model; more complex models would account for, e.g., nonpolynomial dependencies on the relative speed, pressure effects, and other forces such as lift. With the vehicle dynamics specified, we now define the three common classes of optimal path planning problems.

2.1.1. Time optimal path planning with an energy constraint

In time optimal path planning, the vehicle is tasked with reaching the destination in minimal time. Here, we augment this problem by adding a constraint on the energy usage and require that the vehicle arrive at the destination with at least some amount of energy remaining e_{min}. Denoting the final time, or time of arrival, by $t_f(F, \hat{\boldsymbol{h}})$, the constrained optimization problem for minimal arrival time is defined as,

$$\begin{aligned} \underset{F(t),\ \hat{\boldsymbol{h}}(t)}{\text{minimize}} \quad & t_f \\ \text{subject to} \quad & E_p(t_f) \geq e_{min} \\ & \text{Eqs. (1a–d)} \\ & \text{Eqs. (2a–b)} \end{aligned} \tag{3}$$

2.1.2. Energy optimal path planning with a time constraint

Alternatively, the dual problem is energy optimal path planning where the vehicle is now tasked with reaching with maximum amount of energy remaining – that is equivalent to minimizing the total energy used – but with a constraint of specified maximum time of arrival t_{max}. Denoting the energy remaining upon reaching the target as $e_f(F, \hat{\boldsymbol{h}})$, this constrained optimization problem for minimum energy usage is defined as,

$$\begin{aligned} \underset{F(t),\ \hat{\boldsymbol{h}}(t)}{\text{maximize}} \quad & e_f \\ \text{subject to} \quad & t_f \leq t_{max} \\ & \text{Eqs. (1a–d)} \\ & \text{Eqs. (2a–b)} \end{aligned} \tag{4}$$

2.1.3. Multi-objective energy–time optimal path planning

The above two cases fall under the general class of multi-objective path planning. In particular, if we consider the two objectives jointly, minimizing arrival time and maximizing the energy remaining (equivalent to minimizing the negative of the energy), we define the multi-objective optimization problem as,

$$\begin{aligned} &\underset{F(t),\ \hat{\boldsymbol{h}}(t)}{\text{minimize}} && [t_f, -e_f] \\ &\text{subject to} && \text{Eqs. (1a–d)} \\ &&& \text{Eqs. (2a–b)} \end{aligned} \tag{5}$$

In this case, the aim is to find the Pareto optimal solutions (the Pareto front) of the optimization problem.

As the optimization problems (3) and (4) define specific Pareto optimal solutions of the above general class, in this work we focus primarily on solving problem (5). Additionally, as we will show, our equations govern *exact* solutions on the Pareto front. Once a Pareto optimal solution from this set is chosen (e.g., when a user selects a desired time to reach and a remaining energy at destination), our methodology predicts the optimal controls and optimal path(s) through the dynamic flow environment.

3. Theory

We now obtain the governing equations for energy–time optimal path planning. In Section 3.1, we review key concepts from control theory and reachability for time optimality. In Section 3.2, we derive the new energy–time optimal equations.

3.1. Time optimal path planning: Control and reachability

For time optimality, all parameters are as in Section 2.1, but the only constraints are (1a, c) and relevant dynamics is the vehicle's motion and trajectory through the physical space, Eq. (2a).

Central to this problem is the evolution of the *reachable set* of the vehicle [34]. Denoted as $\mathcal{R}(\boldsymbol{x}_s, t)$, the reachable set then contains all of the states in the physical space that can be reached at a time t when starting from state $\boldsymbol{x}_s$ at initial time $t = 0$ and using a valid sequence of controls (speed and heading functions). The boundary of this set, $\partial\mathcal{R}(\boldsymbol{x}_s, t)$, is termed the *reachability front*, and intuitively represents the furthest points in space the vehicle can reach at a given time. Once this front reaches the target, a point that remained on the front and reached the target corresponds to a time optimal path. Therefore, with the concepts of reachability, the time optimal path problem consists of evolving the reachability front forward until it reaches the target and then evolving a corresponding trajectory backward until coming back to the start point.

Computing and evolving the reachability front is thus central to time optimal path planning. To do this, the level set method [7,57] has proven to be quite effective. The reachability front $\partial\mathcal{R}(\boldsymbol{x}_s, t)$ – which is a hyper-surface of dimension $\mathbb{R}^{d-1}$ if the physical space is given by $\boldsymbol{x} \in \mathbb{R}^d$ – is then represented by the zero level surface of an implicit function $\phi(\boldsymbol{x}, t)$. Similarly, the initial reachability front – the reachability front at the time $t = 0$ – is represented by the zero level set of a function $\phi_0(\boldsymbol{x})$. At time $t = 0$, the only state that is reachable is the starting state and hence the initial reachable set only contains this state, i.e. $\mathcal{R}(\boldsymbol{x}_s, t = 0) = \{\boldsymbol{x}_s\}$. Due to this, $\phi_0(\boldsymbol{x})$ can be defined as a signed distance function relative to $\boldsymbol{x}_s$ and the reachable set $\mathcal{R}(\boldsymbol{x}_s, t)$ is then the set of locations where $\phi(\boldsymbol{x}, t)$ is zero or negative. As developed in [8,35], for suitable Lipschitz conditions, the evolution of $\phi(\boldsymbol{x}, t)$ is governed by the Hamilton–Jacobi PDE:

$$\begin{aligned} \frac{\partial\phi(\boldsymbol{x}, t)}{\partial t} + \max_{F, \hat{\boldsymbol{h}}} \left\{ F\, \hat{\boldsymbol{h}}^T \cdot \frac{\partial\phi}{\partial \boldsymbol{x}} \right\} + \boldsymbol{V}(\boldsymbol{x}, t) \cdot \frac{\partial\phi}{\partial \boldsymbol{x}} = 0, \\ \phi(\boldsymbol{x}, t = 0) = \phi_0. \end{aligned} \tag{6}$$

In (6), we used $\frac{\partial\phi}{\partial \boldsymbol{x}} \in \mathbb{R}^d$ to denote the generalized spatial gradient vector. The solution to (6) gives $\phi(\boldsymbol{x}, t)$ whose zero level set at any given time yields the reachability front $\partial\mathcal{R}(\boldsymbol{x}_s, t)$.

The maximization in (6) can be performed analytically. In particular, if the speed function is bounded as $F \in [0, F_{max}]$, we have that the optimal speed and heading is given, at any point in space and time, as $F^*(\boldsymbol{x}, t) = F_{max}$

and $\hat{\boldsymbol{h}}^*(\boldsymbol{x},t) = \frac{\frac{\partial\phi}{\partial\boldsymbol{x}}\big|_{(\boldsymbol{x},t)}}{\left\|\frac{\partial\phi}{\partial\boldsymbol{x}}\big|_{(\boldsymbol{x},t)}\right\|}$, respectively, resulting in the following PDE governing the evolution of the reachability front:

$$\frac{\partial\phi(\boldsymbol{x},t)}{\partial t} + F_{max}\left\|\frac{\partial\phi}{\partial\boldsymbol{x}}\right\| + \boldsymbol{V}(\boldsymbol{x},t)\cdot\frac{\partial\phi}{\partial\boldsymbol{x}} = 0,$$
$$\phi(\boldsymbol{x},t=0) = \phi_0. \tag{7}$$

Eq. (7) is solved until the time t_f such that $\phi(\boldsymbol{x}_f,t_f)=0$. In other words, the equation is solved until the first time the reachability front reaches the target. If this condition does not occur, it implies that the target state is not reachable. We also note that we are using a closed-loop control law and as such, our controls depend on both the present time and position of the vehicle.

Once the reachability front has reached the destination, using the evolved $\phi(\boldsymbol{x},t)$, the optimal path is determined by solving Eq. (2a) backward in time. Specifically, for the fastest growth of the reachable set, the optimal heading is always normal to the reachability front and the optimal speed is F_{max} [7,35], such that the optimal path $\boldsymbol{X}_p^*(t)$ is governed by,

$$\frac{\mathrm{d}\boldsymbol{X}_p^*}{\mathrm{d}t} = -\boldsymbol{V}(\boldsymbol{X}_p^*(t),t) - F_{max}\cdot\frac{\frac{\partial\phi}{\partial\boldsymbol{x}}\big|_{(\boldsymbol{X}_p^*(t),t)}}{\left\|\frac{\partial\phi}{\partial\boldsymbol{x}}\big|_{(\boldsymbol{X}_p^*(t),t)}\right\|}. \tag{8}$$

Eq. (8) is solved backward in time starting from $\boldsymbol{X}_p^*(t=t_f)=\boldsymbol{x}_f$ to $\boldsymbol{X}_p^*(0)=\boldsymbol{x}_s$. It is referred to as the backtracking equation and returns the globally time-optimal path from the start point to the destination. Eq. (8) is in fact the characteristic equation of the reachability PDE (Eq. (7)). Actuating in the normal direction to the reachability front ensures that you stay on it. We remark that these equations were used and validated in real-time at-sea experiments. Using ocean forecasts as inputs, the AUVs using our time-optimal path forecasts reached their targets first, winning all races, even though the ocean flows were complex [58]. Our equations also provided skillful reachability forecasts for real floats and gliders during the Northern Arabian Sea Circulation-Autonomous Research (NASCar) experiment [59,60].

3.2. Multi-objective energy–time optimal path planning

We now derive the equations for energy–time optimal path planning including the forward PDE, Pareto front, and backtracking ODE. Central to addressing this problem will be a reachability analysis of the system in an *augmented state space* involving the vehicle's spatial position and available energy.

3.2.1. Energy–time forward reachability PDE

To derive the differential equations governing the evolution of the reachability front in the energy–time space, we start from the dynamics of the vehicle in the physical space, Eq. (2a), and the dynamics in the energy space, Eq. (2b). We define the augmented state space, $\Omega^{\boldsymbol{a}}\subseteq\mathbb{R}^{d+1}$, whose coordinates $\boldsymbol{x}^{\boldsymbol{a}}=[\boldsymbol{x}\ e]^T\in\mathbb{R}^{d+1}$ consist of the spatial position and energy states of the vehicle. For a specified control policy given by the heading function, $\hat{\boldsymbol{h}}(\boldsymbol{X}_p,E_p,t)$, and speed function, $F(\boldsymbol{X}_p,E_p,t)$, the augmented state trajectory of the vehicle in $\Omega^{\boldsymbol{a}}$, $\boldsymbol{X}_p^{\boldsymbol{a}}(t)\in\mathbb{R}^{d+1}$, is governed by the ODE system,

$$\frac{\mathrm{d}\boldsymbol{X}_p^{\boldsymbol{a}}(t)}{\mathrm{d}t} = \boldsymbol{U}^{\boldsymbol{a}}(\boldsymbol{X}_p^{\boldsymbol{a}}(t),t) + \boldsymbol{V}^{\boldsymbol{a}}\left(\boldsymbol{X}_p^{\boldsymbol{a}}(t),t\right), \tag{9}$$

where

$$\boldsymbol{X}_p^{\boldsymbol{a}} = \begin{bmatrix}\boldsymbol{X}_p\\ E_p\end{bmatrix}, \tag{10a}$$

$$\boldsymbol{U}^{\boldsymbol{a}}(\boldsymbol{X}_p^{\boldsymbol{a}}(t),t) = \begin{bmatrix}F(\boldsymbol{X}_p^{\boldsymbol{a}},t)\,\hat{\boldsymbol{h}}(\boldsymbol{X}_p^{\boldsymbol{a}},t)\\ -\dot{W}(F(\boldsymbol{X}_p^{\boldsymbol{a}},t))\end{bmatrix}, \tag{10b}$$

$$\boldsymbol{V}^{\boldsymbol{a}}\left(\boldsymbol{X}_p^{\boldsymbol{a}}(t),t\right) = \begin{bmatrix}\boldsymbol{V}\left(\boldsymbol{X}_p,t\right)\\ 0\end{bmatrix}. \tag{10c}$$

In the augmented state space Ω^a, the initial position and energy level of the vehicle at the start point is $\boldsymbol{x}_s^a = [\boldsymbol{x}_s, e_s]^T$. Our goal is to determine the PDE that governs the evolution of the augmented reachable set and reachability front in Ω^a, i.e., $\mathcal{R}(\boldsymbol{x}_s^a, t)$ and $\partial\mathcal{R}(\boldsymbol{x}_s^a, t)$. This PDE governs the set of all the points in Ω^a (spatial position and energy level of the vehicle) that are reachable at any arbitrary time t.

To obtain the evolution of the reachable set and reachability front in Ω^a, we analyze the ODEs Eq. (9) in the context of *characteristics* of a PDE. In particular, under sufficient regularity conditions [61,62] on the augmented "velocity" field, $\boldsymbol{U}^a + \boldsymbol{V}^a$, the ODEs Eq. (9) determine the characteristic curves of a generalized advection PDE defined in Ω^a,

$$\frac{\partial\phi(\boldsymbol{x}^a, t)}{\partial t} + \left(\boldsymbol{U}^a(\boldsymbol{x}^a, t) + \boldsymbol{V}^a(\boldsymbol{x}^a, t)\right) \cdot \frac{\partial\phi}{\partial \boldsymbol{x}^a} = 0. \tag{11}$$

The value of ϕ obtained by solving this PDE will be constant along trajectories governed by ODEs Eq. (9) – in other words, ϕ is constant along the augmented characteristic curves.

Every point on the reachability front can be reached by a vehicle under some set of controls (by definition). Let $F^*(\boldsymbol{x}^a, t)$ and $\hat{\boldsymbol{h}}^*(\boldsymbol{x}^a, t)$ be optimal controls that keep a vehicle on the reachability front. Substituting the corresponding $\boldsymbol{U}^{a*}(\boldsymbol{x}^a, t)$ in Eq. (11), we obtain a PDE whose characteristics are the dynamics of vehicles that remain on the augmented reachability front,

$$\frac{\partial\phi(\boldsymbol{x}^a, t)}{\partial t} + \left(\boldsymbol{U}^{a*}(\boldsymbol{x}^a, t) + \boldsymbol{V}^a(\boldsymbol{x}^a, t)\right) \cdot \frac{\partial\phi}{\partial \boldsymbol{x}^a} = 0. \tag{12}$$

If the initial field $\phi_0(\boldsymbol{x}^a)$ has a zero contour set to the initial reachability front $\partial\mathcal{R}(\boldsymbol{x}_s^a, 0)$, the PDE (12) will govern the evolution of $\phi(\boldsymbol{x}^a, t)$ such that its zero contour always is the augmented reachability front.

We now define the optimal controls in PDE (12), F^* and $\hat{\boldsymbol{h}}^*$, that maximize the growth of the zero contour and thus lead to the evolution of the reachability front. These optimal controls are obtained by $\arg\max_{F,\hat{\boldsymbol{h}}} (\boldsymbol{U}^a(t) + \boldsymbol{V}^a(\boldsymbol{x}, t)) \cdot \frac{\partial\phi}{\partial \boldsymbol{x}^a}$ because this choice of F^* and $\hat{\boldsymbol{h}}^*$ maximally decreases ϕ at every point in Ω^a and subsequently maximally increases the growth of the reachable region (given by $\phi \leq 0$). Thus, by maximizing the reachable set while respecting the physical-energy constraints, we obtain the augmented Hamilton–Jacobi differential equation governing the evolution of the augmented reachable set and its front:

$$\begin{aligned} &\frac{\partial\phi(\boldsymbol{x}^a, t)}{\partial t} + \max_{\hat{\boldsymbol{h}}, F} \underbrace{\left\{ \boldsymbol{U}^a(\boldsymbol{x}^a, t) \cdot \frac{\partial\phi}{\partial \boldsymbol{x}^a} \right\}}_{\text{Maximization term}} + \boldsymbol{V}^a(\boldsymbol{x}^a, t) \cdot \frac{\partial\phi}{\partial \boldsymbol{x}^a} = 0 \\ \implies &\frac{\partial\phi(\boldsymbol{x}^a, t)}{\partial t} + \max_{\hat{\boldsymbol{h}}, F} \left\{ F\, \hat{\boldsymbol{h}}^T \cdot \frac{\partial\phi}{\partial \boldsymbol{x}} - \dot{W}(F) \cdot \frac{\partial\phi}{\partial e} \right\} + \boldsymbol{V} \cdot \frac{\partial\phi}{\partial \boldsymbol{x}} = 0 \\ &\phi(\boldsymbol{x}^a, t = 0) = \phi_0(\boldsymbol{x}^a) \end{aligned} \tag{13}$$

The novel general PDE (13) extends (6) to higher-dimensional reachability in the augmented space-energy domain, see Fig. 2. As for (6), the initial condition ϕ_0 is set such that its zero contour corresponds to the system's initial reachability front, i.e. ϕ_0 is given by a signed distance function relative to the initial state $\boldsymbol{x}_s^a$ such that the initial reachable set holds just the state $\{\boldsymbol{x}_s^a\}$. Furthermore, the PDE (13) governs the growth of the reachability front using an implicit function that lives in the state space Ω^a of augmented points $\boldsymbol{x}^a = [\boldsymbol{x}\ e]^T \in \mathbb{R}^{d+1}$. At any point in time t, the zero level set of the field $\phi(\boldsymbol{x}^a, t)$ will correspond to the reachability front $\partial\mathcal{R}(\boldsymbol{x}_s^a, t)$. We summarize the main notation for the governing equations in Table 2.

Maximization of the Hamiltonian

What remains to be addressed is the maximization term in Eq. (13). For autonomous vehicles with energy usage models $\dot{W}(F)$ of certain functional forms, this maximization problem can be solved analytically. As motivated in Section 2.1, we consider here a power law for the energy usage of the form $\dot{W}(F) = k \cdot F^n$ where k is a positive proportionality constant and n a positive integer. The maximization term then becomes:

$$\max_{\hat{\boldsymbol{h}}, F} \left\{ F\, \hat{\boldsymbol{h}}^T \cdot \frac{\partial\phi}{\partial \boldsymbol{x}} - k \cdot F^n \cdot \frac{\partial\phi}{\partial e} \right\}. \tag{14}$$

Table 2
Main notation for energy–time path planning.

$\boldsymbol{x^a}$	Augmented energy and physical-space coordinate vector: $[\boldsymbol{x}\,,\ e]$	$\boldsymbol{X^a_p}(t)$	Augmented vehicle state: $[\boldsymbol{X_p}\,,\ E_p]$ i.e., position and energy at time t
$\boldsymbol{x^a_s}$	Start state in the augmented state space	$\boldsymbol{V^a}(\boldsymbol{x^a}, t)$	Augmented flow field
$\mathcal{R}(\boldsymbol{x^a_s}, t)$	Reachable set of states at time t for a system starting at state $\boldsymbol{x^a_s}$ at time $t = 0$	$\boldsymbol{U^a}(\boldsymbol{x^a}, t)$	Augmented control vector $[\,F\,\hat{\boldsymbol{h}}\,,\ -\dot{W}(F)\,]$
$\partial\mathcal{R}(\boldsymbol{x^a_s}, t)$	Reachability front (boundary of the reachable set) at time t	$\phi(\boldsymbol{x^a}, t)$	Implicit function whose zero level surface corresponds to $\partial\mathcal{R}(\boldsymbol{x^a_s}, t)$
$\phi_0(\boldsymbol{x^a})$	Initial implicit function whose zero level surface corresponds to $\partial\mathcal{R}(\boldsymbol{x^a_s}, 0)$	$\frac{\partial\phi}{\partial\boldsymbol{x^a}} \in \mathbb{R}^{d+1}$	Generalized spatial gradient vector
$F^*(\boldsymbol{x^a}, t)$	Optimal control (speed) that maximally grows the reachability set	$\hat{h}^*(\boldsymbol{x^a}, t)$	Optimal control (heading) that maximally grows the reachability set

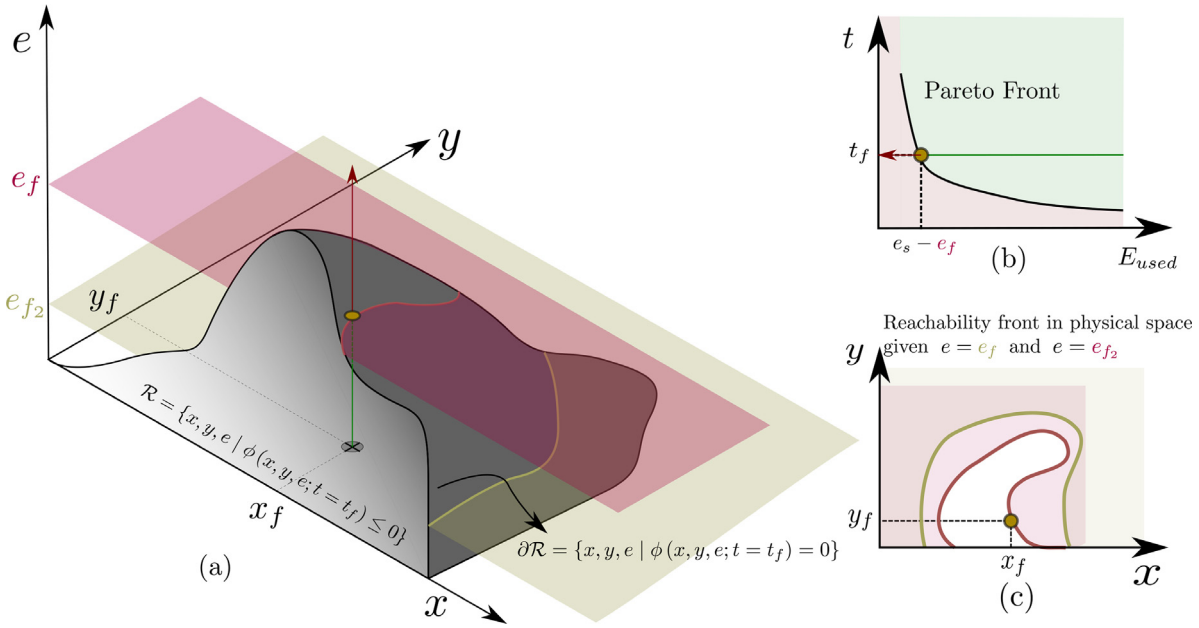

Fig. 2. Augmented reachability front and Pareto front schematics. (a) Evolution of the reachability front in the augmented state space. (b) Pareto front which can be computed by tracking the intersection of the level set with the energy line at the destination. (c) Contours of the reachability front at different energy levels projected onto the physical space. For these schematics, we assumed a three-dimensional (3D) augmented space thus a two-dimensional (2D) physical space.

We first consider the optimization of the heading $\hat{\boldsymbol{h}}$. At any point in the augmented state space and time, it is clear that, based on the properties of the Euclidean dot product, that the optimal heading is given by,

$$\hat{\boldsymbol{h}}^*(\boldsymbol{x}, e, t) = \frac{\frac{\partial\phi}{\partial\boldsymbol{x}}\big|_{(\boldsymbol{x},e,t)}}{\left\|\frac{\partial\phi}{\partial\boldsymbol{x}}\big|_{(\boldsymbol{x},e,t)}\right\|}\,. \tag{15}$$

Substituting this heading $\hat{\boldsymbol{h}}^*$, we are left with,

$$\max_{F\in[0,F_{max}]} \underbrace{\left\{F\left\|\frac{\partial\phi}{\partial\boldsymbol{x}}\right\| - k\cdot F^n\cdot\frac{\partial\phi}{\partial e}\right\}}_{g(F)}, \tag{16}$$

hence a function only of F, $g(F)$, to be maximized. Importantly, the optimal F^* from Eq. (16) will vary in time within $\Omega^{\boldsymbol{a}}$, i.e. we will obtain $F^*(\boldsymbol{x}, e, t)$, because the gradient of ϕ varies in $\Omega^{\boldsymbol{a}}$ and time. In the following, we consider an arbitrary fixed point in $\Omega^{\boldsymbol{a}}$ and maximize the objective $g(F)$ at that point. As $g(F)$ is a polynomial with

parameter n, its maximum admits an analytical solution for the different positive integer n considered. Specifically, there are two cases: (i) $n \geq 2$ and (ii) $n = 1$.

(i) Case $n \geq 2$

For the case of $n \geq 2$, to maximize $g(F)$, we evaluate the derivatives $g'(F)$ and $g''(F)$, and set $g'(\tilde{F}) = 0$,

$$g(F) = F \left\| \frac{\partial \phi}{\partial \boldsymbol{x}} \right\| - k \cdot F^n \cdot \frac{\partial \phi}{\partial e} \tag{17}$$

$$g'(F) = \left\| \frac{\partial \phi}{\partial \boldsymbol{x}} \right\| - k \cdot n \cdot \frac{\partial \phi}{\partial e} \cdot F^{n-1} \tag{18}$$

$$g''(F) = -k \cdot n \cdot (n-1) \cdot \frac{\partial \phi}{\partial e} \cdot F^{n-2} \tag{19}$$

$$g'(\tilde{F}) = 0 \implies \tilde{F} = \left(\frac{\left\| \frac{\partial \phi}{\partial \boldsymbol{x}} \right\|}{k \cdot n \frac{\partial \phi}{\partial e}} \right)^{\frac{1}{n-1}} . \tag{20}$$

Our aim is to determine F^* in the bounded domain $[0, F_{max}]$ that maximizes $g(F)$. To do this, we consider two sub-cases: (a) $\frac{\partial \phi}{\partial e} > 0$ and (b) $\frac{\partial \phi}{\partial e} \leq 0$:

- **(a)** $\frac{\partial \phi}{\partial e} > 0$: Eq. (19) then implies that the polynomial $g(F)$ attains a maximum on the *unbounded* domain for F. This maximum will, furthermore, occur at the unique value of $\tilde{F}$ as given in Eq. (20) and it is important to note that it will be non-negative. If $\tilde{F} \in [0, F_{max}]$, then we simply have that $F^* = \tilde{F}$. When $\tilde{F} > F_{max}$, the maximum would occur beyond the feasible range and the maximizing speed is limited to $F^* = F_{max}$.
- **(b)** $\frac{\partial \phi}{\partial e} \leq 0$: The maximum is then at one of the end points of the interval which, from Eq. (17), can be concluded to occur at $F^* = F_{max}$.

These conditions can all be compiled concisely to give the following for F^*, the optimal speed which maximizes $g(F)$:

$$\max_{F \in [0, F_{max}]} \{ g(F) \} = g(F^*) \tag{21}$$

$$\text{where } F^*(\boldsymbol{x}, e, t) = \begin{cases} F_{max} & \text{if } \frac{\partial \phi}{\partial e} \leq 0 \\ \min \left(F_{max}, \left(\frac{\left\| \frac{\partial \phi}{\partial \boldsymbol{x}} \right\|}{k \cdot n \frac{\partial \phi}{\partial e}} \right)^{\frac{1}{n-1}} \right) & \text{if } \frac{\partial \phi}{\partial e} > 0. \end{cases} \tag{22}$$

(ii) Case $n = 1$

For the case of linear energy usage, we have that

$$g(F) = F \left(\left\| \frac{\partial \phi}{\partial \boldsymbol{x}} \right\| - k \, \frac{\partial \phi}{\partial e} \right). \tag{23}$$

Eq. (23) is a linear function whose maximum can be trivially calculated for F^*, the optimal speed:

$$\max_{F \in [0, F_{max}]} \{ g(F) \} = g(F^*) \tag{24}$$

$$\text{where } F^*(\boldsymbol{x}, e, t) = \begin{cases} F_{max} & \text{if } \left\| \frac{\partial \phi}{\partial \boldsymbol{x}} \right\| \geq k \cdot \frac{\partial \phi}{\partial e} \\ 0 & \text{if } \left\| \frac{\partial \phi}{\partial \boldsymbol{x}} \right\| < k \cdot \frac{\partial \phi}{\partial e}. \end{cases} \tag{25}$$

Final multi-objective energy–time optimal path planning reachability PDE

Substituting in Eq. (13) the optimal speed $F^*(\boldsymbol{x}, e, t)$ – either Eq. (22) or (25) depending on the energy usage model – and the optimal heading Eq. (15), we obtain the PDE governing the evolution of the energy–time reachable set:

$$\frac{\partial \phi(\boldsymbol{x}^{\boldsymbol{a}}, t)}{\partial t} + F^*(\boldsymbol{x}, e, t) \left\| \frac{\partial \phi}{\partial \boldsymbol{x}} \right\| + \boldsymbol{V}(\boldsymbol{x}, t)^T \cdot \frac{\partial \phi}{\partial \boldsymbol{x}} + \left[-k \cdot [F^*(\boldsymbol{x}, e, t)]^n \right] \cdot \frac{\partial \phi}{\partial e} = 0,$$

$$\phi(\boldsymbol{x}^{\boldsymbol{a}}, t = 0) = \phi_0(\boldsymbol{x}^{\boldsymbol{a}}). \tag{26}$$

To reiterate, the reachable set is the set of all states (spatial position and energy level) that the vehicle deployed from the start point (with some initial energy) can be in at any given time. The reachability front is simply the boundary of this set. At a given time t, any point in the reachable set or on the reachability front in the augmented state space is a reachable *state*, that is, controls exist such that the vehicle can reach the specified physical position with the specified energy at that time. To the best of our knowledge, this is the first time Eq. (26) has been derived and presented.

3.2.2. Energy–time pareto front

Our results determine the set of Pareto optimal solutions, i.e. the Pareto front, to the multi-objective energy–time optimal path planning optimization (5). This set of Pareto solutions can be found exactly using the augmented reachable set governed by the PDE (26) or, in general, by the PDE (13).

Key to determining the Pareto front is to track the evolution of the *implicit function*, $\phi(\boldsymbol{x}^{\boldsymbol{a}}, t)$, projected onto the destination point $\boldsymbol{x}_f$ in the physical spatial space, see Fig. 2. Doing so will give us a set of feasible states the vehicle can be in at the destination point at all times. We denote this set of feasible states at destination by $\mathcal{F}_{\boldsymbol{x}_f}$. Given the definition of reachability, we can compute this set,

$$\mathcal{F}_{\boldsymbol{x}_f} = \{(e, t) \mid \phi(\boldsymbol{x}_f, e, t) \leq 0\}. \tag{27}$$

The feasibility set given in (27) will include all the energy and time values at which the vehicle can reach the destination. Given that these are the two quantities we are trying to optimize, we can compute the set of Pareto optimal solutions, $\mathcal{P}$, given this feasibility set. These will be all the solutions in the feasibility set such that no other point with a lower time and a higher energy available at destination exists in the set,

$$\mathcal{P} = \left\{(e, t) \in \mathcal{F}_{\boldsymbol{x}_f} \;\middle|\; \left\{(e', t') \in \mathcal{F}_{\boldsymbol{x}_f} \mid e' \geq e \text{ and } t' \leq t\right\} = \{(e, t)\}\right\}. \tag{28}$$

Further details on how to compute this Pareto front are included in Appendix A.2.

3.2.3. Energy–time backtracking

Once the Pareto front has been generated, any Pareto optimal solution can be selected by a decision maker who expresses preference for their objectives of interest, e.g., what tradeoff between the final vehicle energy remaining and the arrival time. Consider an arbitrary Pareto optimal solution (t_f^*, e_f^*) to the energy–time optimization problem. The optimal path, $\boldsymbol{X}_{\boldsymbol{p}}^{\boldsymbol{a},*}(t)$, corresponding to this solution is obtained using the optimal controls and the vehicle dynamics, solving the augmented backtracking ODE system. Specifically, the following backtracking ODE system in the *augmented* state space determines the optimal path,

$$\frac{\mathrm{d}\boldsymbol{X}_{\boldsymbol{p}}^{\boldsymbol{a},*}}{\mathrm{d}t} = -\boldsymbol{U}_*^{\boldsymbol{a}}(\boldsymbol{X}_{\boldsymbol{p}}^{\boldsymbol{a},*}(t), t) - \boldsymbol{V}^{\boldsymbol{a}}(\boldsymbol{X}_{\boldsymbol{p}}^{\boldsymbol{a},*}(t), t)\,, \tag{29}$$

where

$$\boldsymbol{X}_{\boldsymbol{p}}^{\boldsymbol{a},*} = \begin{bmatrix} \boldsymbol{X}_{\boldsymbol{p}}^* \\ E_p^* \end{bmatrix} \tag{30a}$$

$$\boldsymbol{U}_*^{\boldsymbol{a}}(\boldsymbol{X}_{\boldsymbol{p}}^{\boldsymbol{a},*}(t), t) = \begin{bmatrix} F^*(\boldsymbol{X}_{\boldsymbol{p}}^*(t), E_p^*(t), t) \cdot \hat{\boldsymbol{h}}^*(\boldsymbol{X}_{\boldsymbol{p}}^*(t), E_p^*(t), t) \\ -\dot{W}(F^*(\boldsymbol{X}_{\boldsymbol{p}}^*(t), E_p^*(t), t), t) \end{bmatrix} \tag{30b}$$

$$\boldsymbol{V}^{\boldsymbol{a}}\left(\boldsymbol{X}_{\boldsymbol{p}}^{\boldsymbol{a},*}(t), t\right) = \begin{bmatrix} \boldsymbol{V}\left(\boldsymbol{X}_{\boldsymbol{p}}^{\boldsymbol{a},*}(t), t\right) \\ 0 \end{bmatrix}. \tag{30c}$$

Eq. (29) is solved backward in time starting from $\boldsymbol{X}_{\boldsymbol{p}}^{\boldsymbol{a},*}(t = t_f^*) = [\boldsymbol{x}_f, e_f^*]^T$. Again, the optimal heading $\hat{\boldsymbol{h}}^*$ is given by Eq. (15) and optimal speed F^* by Eq. (22) or (25).

3.3. Summary

We first derived the PDEs governing the reachable set for multi-objective energy–time optimal path planning in dynamic environments, specifically (26) or, in general, (13). Projecting its reachability front onto the destination

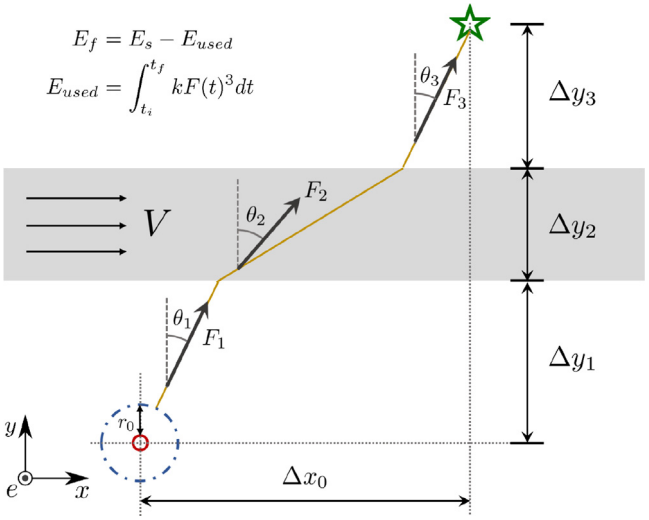

Fig. 3. Schematic describing the problem of finding energy–time optimal paths for crossing a jet flow (or highway). In physical space (x, y), the vehicle has to travel from the start point (○) at time t_i to the destination (★). The environment consists of a steady uniform current of velocity V going horizontally through the middle of the domain, with physical dimensions Δx_0, Δy_1, Δy_2, and Δy_3. The controls F_i and θ_i are the speeds and headings of the vehicle in the three domains (before, in, and after the jet, $i = 1, 2, 3$). In the third dimension, energy e, the final energy of the vehicle E_f at time t_f is the difference between its initial energy E_s and the energy used to make the trip, E_{used}. Finally, r_0 is the radius of the initial set of possible vehicle states in the 3D augmented space, (x, y, e). (For interpretation of the references to color in this figure legend, the reader is referred to the web version of this article.)

point $\boldsymbol{x}_f$ in physical space then provides the feasibility set (27) from which the energy–time Pareto front is easily obtained by direct optimization. Integrating the augmented trajectory ODE system (29) backward in time, along with Eq. (15) for the optimal heading and Eq. (22) or Eq. (25) for the optimal speed, finally provides the optimal paths and optimal controls. All of these equations are exact and their integration thus avoids the need for heuristics. Specifically, they provide exact Pareto optimal solutions to the multi-objective optimal path planning problem. Numerical schemes for solving these equations are presented in Appendix A, specifically for the forward PDE solve Appendix A.1, the Pareto front computation Appendix A.2, and the backtracking ODEs solve Appendix A.3. Overall, the result is a first comprehensive and exact PDE-based methodology for predicting the energy–time optimal paths of autonomous marine vehicles navigating in highly dynamic ocean environments.

4. Applications

In this section, we illustrate our theory and schemes on two numerical applications. The first considers the canonical case of crossing a simple idealized jet. This application admits a semi-analytical solution that is useful to validate our schemes. The second considers energy–time optimal path planning in a dynamic flow to showcase the applicability of our methodology in more complex conditions. In these applications, all values are dimensionless unless otherwise specified. We note that we completed many other simulations (not shown) to validate the results.

4.1. Energy–time optimal for crossing a jet flow

We consider first the case of determining energy–time optimal paths for crossing a simple idealized jet or current as shown in Fig. 3 (figure not to scale). The current, which can be thought of as a "highway", consists of a uniform steady jet that flows from west to east in a rectangular domain. The autonomous vehicle has to traverse from a starting set in the southwest of the domain to a target point in the northeast of the domain, on the other side of the jet. The starting set is a set of states the vehicle can choose to start from in the 3D space, (x, y, e). We consider the set to be a sphere of radius r_0 centered at $[x_s, y_s, e_s]$. The goal is to find energy–time optimal paths – Pareto optimal solutions – for the multi-objective problem of jointly minimizing arrival time and energy usage.

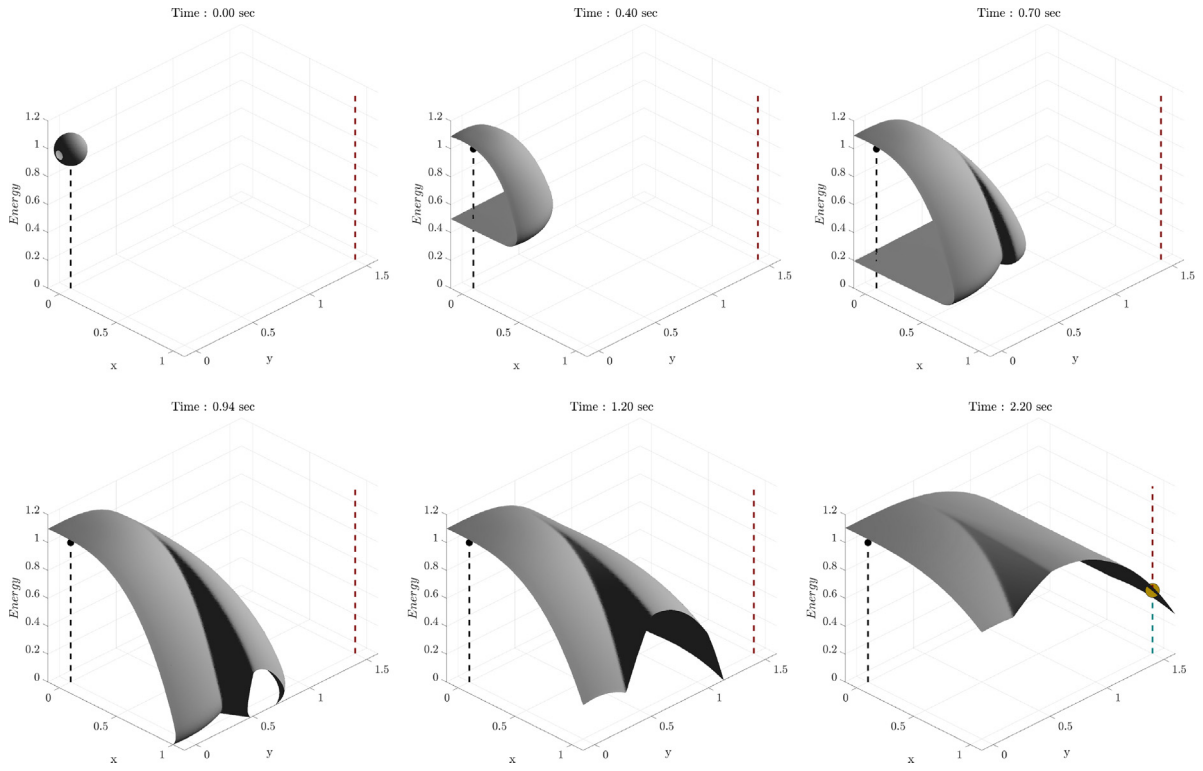

Fig. 4. Crossing a jet flow: Forward solve. Snapshots of the time evolution of the reachability front are shown in the augmented state space consisting of the vehicle's position and its energy level, (x, y, e). At the start time, the reachability front is specified with a small initial sphere around the start state (initial position $(x, y) = (0, 0)$ and energy $E = 1$). In each snapshot, the reachable set corresponds to the set of all states that are enclosed by the front. The dashed black and red vertical lines correspond to the start and destination points, respectively. The part of the destination line shaded green (bottom left panel) corresponds to the energy states that are reachable at the destination at that time snapshot. The front can be seen to stretch in the direction of the external current when it enters the highway region.

Given the low degrees of freedom of the solution, it is possible to compute the optimal solution using traditional optimization techniques. This is discussed in Appendix B.

For the example we show, we selected values of $\Delta y_1 = \Delta y_2 = \Delta y_3 = 0.5$ to define the net vertical distance between the start and target points. The net horizontal distance is $\Delta x_0 = 1.0$. The initial reachable set is considered to be a sphere of radius $r_0 = 0.1$ (set of locations and energies from which the vehicle can start). A cubic energy usage model is used ($\dot{W} \propto F^3$) with an energy dissipation rate of $k = 1.0$ units. We set the maximum speed of the vehicle F_{max} and the speed of the jet V at 1 unit each. Numerically, the domain is discretized using 121, 181, and 76 nodes in the x-axis, y-axis, and e-axis, respectively. To evolve the reachability front in the forward solve, a second order ENO scheme is used for all spatial derivatives and a second order Total Variation Diminishing (TVD) Runge–Kutta scheme for time integration with a fixed time step $\Delta t = 1 \times 10^{-4}$. A first order implicit scheme is finally used – as described in Appendix A.3 – to compute optimal paths corresponding to different Pareto optimal solutions.

Figs. 4 and 5 show the time evolution of the reachability front from the forward solve. Fig. 4 shows a 3D isometric view of this reachability front in the augmented state space, while Fig. 5 depicts the contours of this front as seen in the physical space. As the front evolves, the vehicle can either reach further away by losing energy or stay close to the starting point saving energy. This gives the front the ellipsoid shape as it evolves in the region with no background velocity. Over time, more regions that were initially reachable only by fast moving vehicles become reachable by slower moving vehicles that conserve energy, thus raising the augmented reachability front in the e-direction in those regions. The strong currents in the jet can be seen to deform the reachability front in the jet region in the direction of the current, leading to a sharp front in the e-direction. As time progresses, the reachability

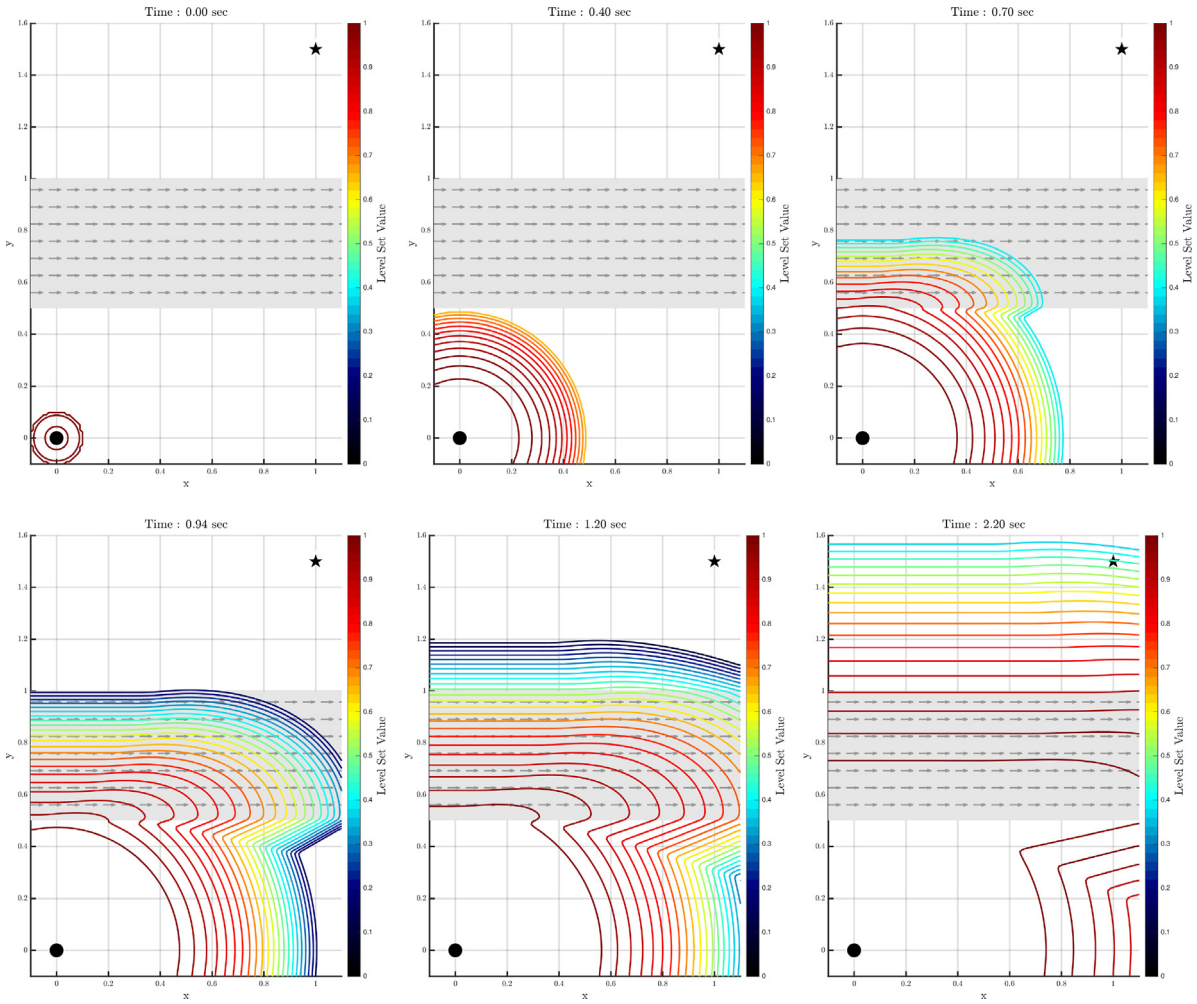

Fig. 5. Crossing a jet flow: Forward solve. Snapshots of the augmented reachability front's evolution in time shown by the contours of the front (at various energy values) projected onto the physical domain, as schematized in Fig. 2(c). The six panels are at the same snapshot times as those shown in Fig. 4. The contours depicted correspond to slices along the energy axis of the 3D reachability fronts shown in Fig. 4. They contain the set of locations the vehicle can reach with the energy given by the color of the contour line.

front continues to rise in the e-direction, but without reaching the limit of the initial energy, as it represents slower and slower vehicles, using less and less energy.

Fig. 6 illustrates the final Pareto energy–time optimal solutions and their validation by comparison to semi-analytical solutions. First, Panel 6(a) shows the Pareto front, containing all possible Pareto optimal solutions that allow the vehicle to reach the destination with optimal travel times and energy used. For validation, we show both the Pareto front computed using our formulation and the semi-analytical Pareto front obtained by solving Eq. (B.5) using numerical optimization software. With the Pareto front computed, we then chose three different Pareto optimal solutions on the front. Specifically, they correspond to energy usage values of 0.8, 0.5, and 0.3. Their optimal paths and optimal speed functions (the speed used by the vehicle as a function of time) are shown in Panels 6(c) and 6(b), respectively. As expected, the optimal paths are all angled in order to leverage the large current from the jet helping the vehicle reach the destination. Additionally, in the jet, the vehicle noticeably reduces its thrust, and thus

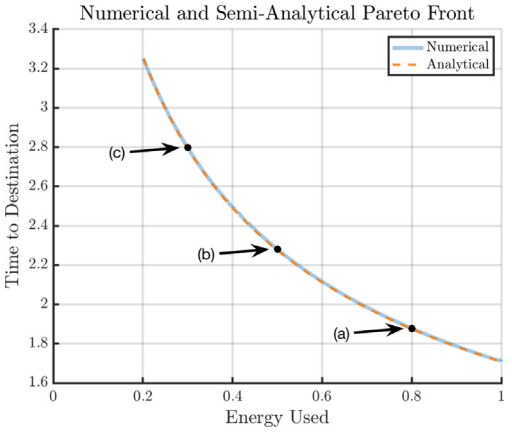

(a) Numerical and semi-analytical Pareto fronts for the multi-objective energy-time optimization. Three different Pareto optimal solutions are selected, as labelled. These three solutions are shown in the optimal paths and optimal speed Panels.

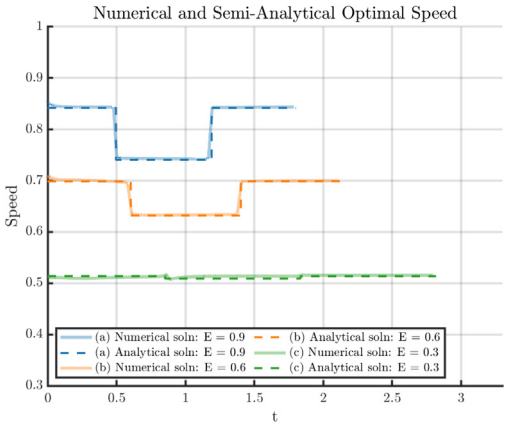

(b) Optimal speed functions: numerical and semi-analytical solutions. The three optimal speed functions correspond to the chosen three Pareto optimal solutions and paths.

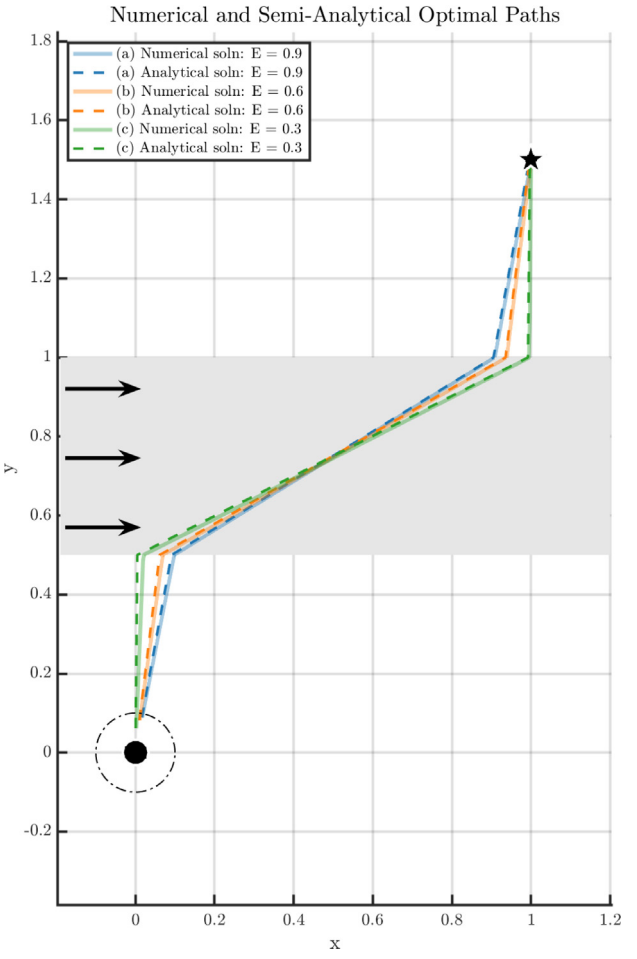

(c) Optimal paths: numerical and semi-analytical solutions. The three optimal paths correspond to the chosen three Pareto optimal solutions and speeds. Shown in the dashed-dot black line is the projection of the initial spherical reachability front onto the physical space.

Fig. 6. Crossing a jet flow: Final Pareto optimal solutions to the multi-objective energy–time optimal path planning.

reduces its energy consumption, as the favorable current can be used to reach the target more efficiently. We again find good agreement in these Figures between our computed optimal solutions and the analytical solutions.

4.2. Double-gyre barotropic quasi-geostrophic ocean circulation

We now consider a more complex, time-dependent environment by considering a simulated double-gyre ocean flow field. This flow represents near-surface ocean circulation at mid-latitude regions, where easterlies and trade winds in the northern hemisphere drive a cyclonic and an anticyclonic gyre with the zonal jet in between (e.g. an idealized version of the Gulf Stream) [7]. It is governed by the following non-dimensional PDEs

$$\frac{\partial u}{\partial t} = \frac{\partial p}{\partial x} + \frac{1}{\mathrm{Re}}\Delta u - \frac{\partial (u^2)}{\partial x} - \frac{\partial (uv)}{\partial y} + fv + a\tau_x$$
$$\frac{\partial v}{\partial t} = \frac{\partial p}{\partial y} + \frac{1}{\mathrm{Re}}\Delta v - \frac{\partial (uv)}{\partial x} - \frac{\partial (v^2)}{\partial y} - fu + a\tau_y$$

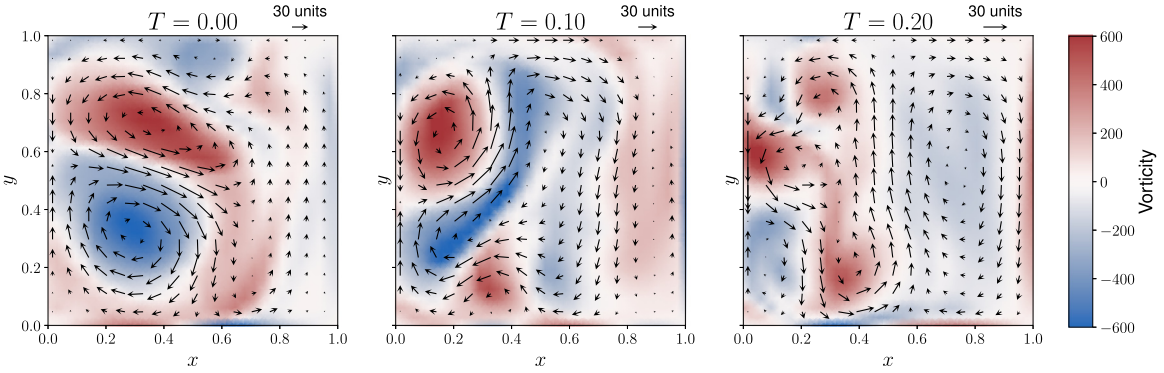

Fig. 7. Snapshots of the quasi-geostrophic double gyre flow field at three non-dimensional times, with non-dimensional flow currents reaching 50 units. The fields of ocean currents are represented by velocity vectors, with the non-dimensional vorticity field colored in the background.

$$0 = \frac{\partial u}{\partial x} + \frac{\partial v}{\partial y}\,. \tag{31}$$

We solve these PDEs numerically using our modular finite volume framework [63]. For the example shown, a flow Reynolds number of 150 was used with $f = \tilde{f} + \beta y$, the non-dimensional Coriolis coefficient with non-dimensional $\tilde{f} = 0$ and $\beta = 10^3$, and finally, $a = 10^3$, the strength of the wind stress. The flow in the basin is forced by an idealized steady zonal wind stress, $\tau_x = -\frac{1}{2\pi} cos\ 2\pi y$ and $\tau_y = 0$. Snapshots of the flow field at various non-dimensional times are shown in Fig. 7, with flow currents reaching values of the order 50 units.

In the example shown, optimal paths were searched for a vehicle launched in the northwest of the domain and tasked with navigating to a destination point at the southeast of the domain, sailing through the dynamic flow field. The augmented reachability front of the vehicle was propagated forward to a non-dimensional time of $t = 0.25$. A cubic energy usage model is again used ($\dot{W} \propto F^3$) with an energy dissipation rate of $k = 0.1$. The maximum velocity of the vehicle was set to $F_{max} = 4$ units. Furthermore, the domain was discretized using 75 nodes along all three coordinate axes (x, y and E). To evolve the reachability front in the forward solve, a second order ENO scheme was used to compute all spatial derivatives and a second order Total Variation Diminishing (TVD) Runge–Kutta scheme to integrate in time with a fixed time step size of $\Delta t = 5 \times 10^{-5}$. Finally, as in the first application, a first order implicit scheme was used to backtrack the optimal paths corresponding to different Pareto optimal solutions.

Fig. 8 shows the time evolution of the energy–time reachability front. Specifically, we again show the contours at various energy values of the reachability front in the augmented space. We find that the strong flow field has a large influence on the propagation of the reachability front. This is especially evidenced at earlier times where the projection of the reachability front in the physical space can be seen to be advected in a circular pattern as a result of the gyre (refer to the snapshots at non-dimensional times 0.02 and 0.04). The front furthermore expands fastest in directions in which it is assisted by the flow field as well. This can be observed for example in the snapshots at non-dimensional times 0.06, 0.08, and 0.10, where the reachability front is carried southward on the edge of a gyre.

Fig. 9 illustrates the final energy–time optimal solution for the dynamic double-gyre flow. Panel 9(a) shows the Pareto front, holding all possible Pareto optimal solutions of varying travel time and vehicle energy usage. This front was computed using the methodology outlined in Section 3.2.2. The dotted red curve was obtained by continuously measuring the maximum energy value of the reachability front at the destination as a function of time. Minimizing time, one then obtains the Pareto front for the multi-objective path planning problem shown in blue. From this Pareto front, we then selected three different Pareto optimal energy and time combinations, and we computed the corresponding optimal controls and optimal paths.

Panels 9(b) and 9(c) show the optimal speeds and paths for these three Pareto optimal solutions, obtained by backtracking from the destination to the start point. The different energy usage values for the Pareto optimal solutions result in the differences in the optimal paths and speed functions of the vehicle. As expected, vehicles with lower energy usage values have slightly slower optimal speeds on average. Moreover, each solution can be seen to have optimal paths that are quite similar near the start point, as they all perform a loop due to the influence of the gyre

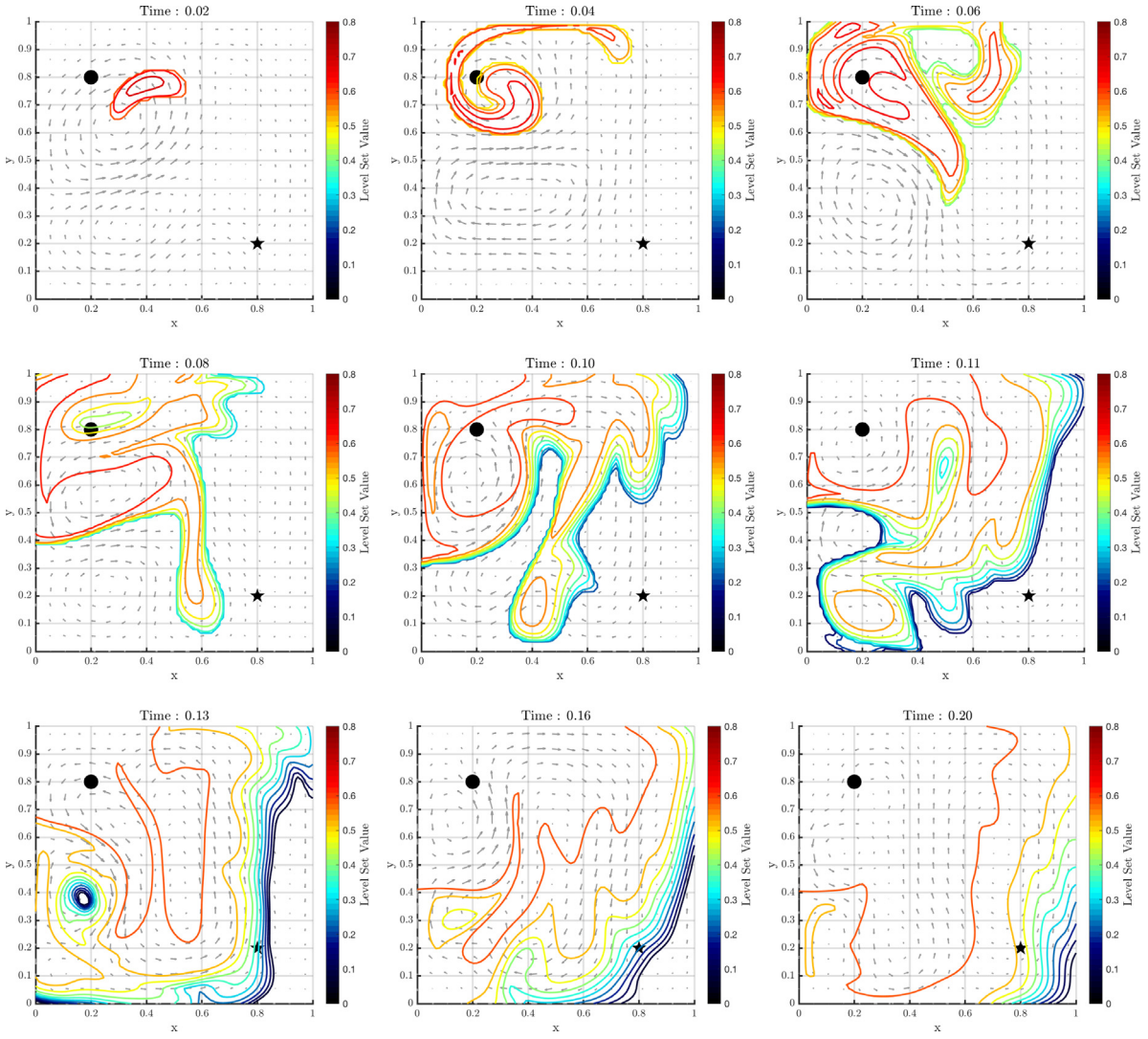

Fig. 8. Dynamic quasi-geostrophic double gyre flow: Forward solve. Snapshots of the evolution of the augmented reachability front. Plotted are the contours of the front at different energy levels projected onto the physical domain and overlaid on the dynamic field of simulated ocean velocity vectors. The reachability front is here a surface in a 3D space (x, y, e), and the contours plotted are slices of this front at different energy values (as schematized in Fig. 2(c)). The start time for the vehicle is $T = 0$, with the start point (circle) and target endpoint (star) as shown.

whose speeds ($\sim$30 units) are larger than the speed of the vehicle ($\sim$4 units). The paths then differ most once they exit this loop, where it can be seen that vehicles with higher energy usage values (and correspondingly higher speeds) take a more direct path to the target, whereas the others which move slower are more strongly influenced by the external velocity field.

5. Conclusions and future work

In this work, we developed new fundamental theory and schemes for joint energy–time optimal path planning of autonomous vehicles navigating in known strong and dynamic flow fields. We started from the kinematic velocity equation in physical space and the first law of thermodynamics in energy space. Augmenting the physical dimensions with the energy dimension, we then obtained the exact PDE governing the energy- and physical-space forward reachable sets for multi-objective energy–time optimization in dynamic environments. Integrating this PDE

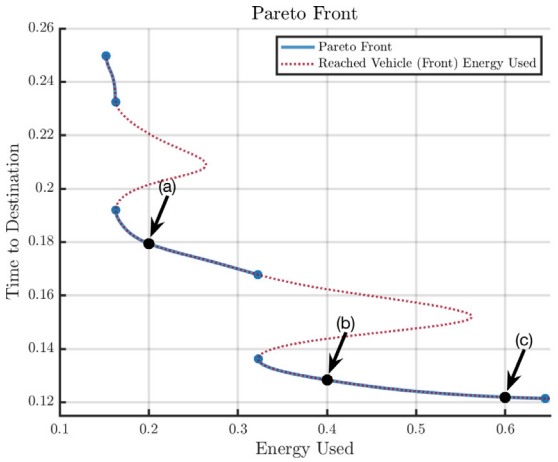

(a) Pareto front for the multi-objective path planning. Three Pareto optimal solutions are marked. Their optimal speed functions and paths are shown in the other Panels.

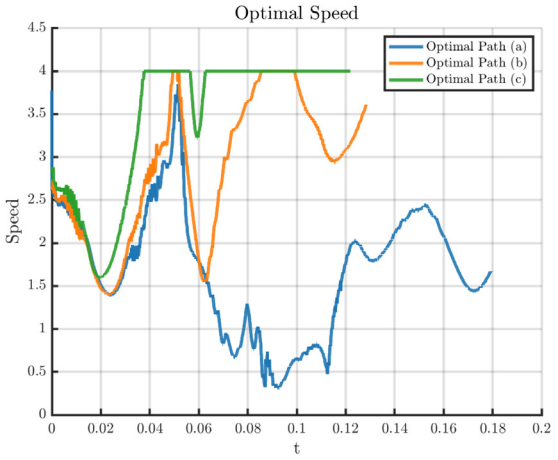

(b) Optimal speed functions for the three marked Pareto optimal solutions.

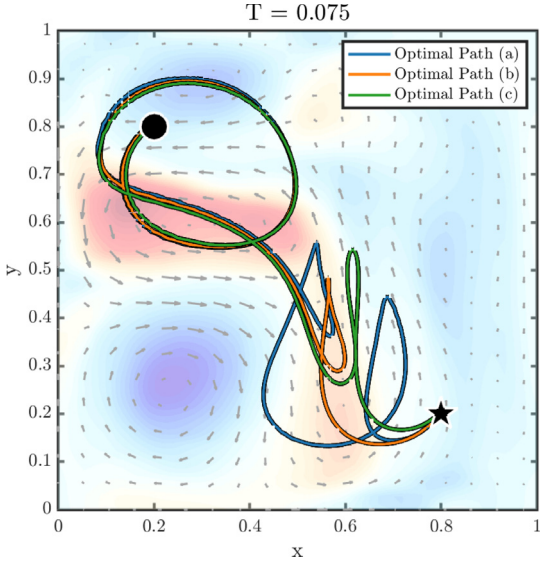

(c) Optimal paths for the three marked Pareto optimal solutions.

Fig. 9. Dynamic quasi-geostrophic double gyre flow: Final Pareto optimal solutions to the energy–time optimal path planning.

and projecting the augmented reachability front onto the destination point in physical space then determines the feasibility set from which the energy–time Pareto front is obtained by direct optimization. Users can then select any Pareto optimal solution(s) that they prefer based on how highly they value minimizing energy usage or travel time, or on some weighted combination of the two. Finally, integrating the augmented trajectory ODE system backward in time, starting from the endpoints of Pareto optimal solution(s), provides the energy–time globally optimal paths as well as the optimal controls, the time evolution of optimal headings and propulsion speeds (power usage). All of these equations are exact and their integration thus avoids the need for heuristics. Specifically, they provide exact Pareto optimal solutions to the multi-objective optimal path planning problem. Computationally, in the forward and backward integrations, dynamic flow fields are used as inputs, e.g. numerical current predictions. The level set method is used to integrate the forward reachability PDE in the augmented spatial and energy domain. Explicit schemes are used for the forward reachable set and reachability front, and implicit schemes for the backward trajectory. Overall, the results are the fundamental differential equations and an efficient methodology for

predicting the energy–time optimal paths and controls of autonomous vehicles navigating in known highly-dynamic environments.

We illustrated our theory and schemes on two numerical applications. The first was a validation example, using the canonical crossing of an idealized jet or highway flow. This example admits a semi-analytical Pareto front and optimal paths solutions which allowed us to verify the correctness of our schemes and implementation. The second considers energy–time optimal path planning in a more complex dynamic flow, a double-gyre barotropic quasi-geostrophic flow that is representative of ocean circulations at mid-latitudes. Results showed that our methodology governs all energy–time optimal solutions and that optimal solutions can be strongly influenced by the complex unsteady flow conditions.

A first advantage of our methodology is that it is based on the exact augmented forward Hamilton–Jacobi PDE and augmented backward trajectory ODE, thus removing the need for heuristics. A second is that it is computationally efficient and, for a given desired accuracy, commonly more efficient than graph methods [50]. A third is that the path planning resolution can be commensurate to that of the flow field available, e.g. that of data assimilative ocean forecasts [58,64–67]. Fourth, it is directly applicable to diverse power usage models. The main assumptions are that the external flow is known and that the dimensions of the vehicle are small compared to the spatial scales of the flow and distance to travel such that the vehicle is modeled as a point particle without inertia.

There are many directions for future advances and applications. First, the extension to moving targets, multiple start points, and obstacle avoidance (islands, forbidden regions, etc.) is relatively straightforward [68]. Second, it can also be extended to vehicles with constrained motions such as floats or gliders [59,69]. Third, the approach is not limited to path planning with two objectives. It can be generalized to the harvesting of external fields, for example, environmental energy harvesting or ocean plastic collection [70–72]. Fourth, all examples considered assumed complete knowledge of the flow fields, that is, only known deterministic environmental fields were used. Such exact knowledge is rarely available, and a truly robust scheme should apply to uncertain flows. To do so, our energy–time optimal differential equations can remain the governing equations but with stochastic flow field inputs, i.e., the results in [59,73,74] are used for stochastic risk-energy–time optimal path planning. Fifth, the predictions from our theory and schemes should be used in sea experiments [5] and can be merged with real-time observations for onboard planning [75]. As a vehicle travels to the target, it would then utilize and assimilate measurements to improve the ocean field predictions and modify or recompute its optimal path prediction accordingly. Sixth, our energy–time schemes can be used for or combined with other goals such as optimal monitoring or adaptive sampling [5,76–78]. Finally, our results are applicable to varied dynamic environments and applications [32,79–82].

Declaration of competing interest

The authors declare that they have no known competing financial interests or personal relationships that could have appeared to influence the work reported in this paper.

Data availability

No data was used for the research described in the article.

Acknowledgments

We thank the members of our MSEAS group for insightful discussions. We are grateful to the Office of Naval Research, United States of America for partial support under Grant N00014-14-1-0476 (Science of Autonomy LEARNS) to the Massachusetts Institute of Technology (MIT), United States of America as well as to the MIT Portugal Program for support under a MPP seed project and a Flagship program project (K2D).

Appendix A. Numerical schemes and implementation

As discussed in Section 3, our optimal path planning methodology is composed of two primary steps. The first involves the evolution of the augmented reachability front and corresponding Pareto front, and is denoted as the *forward solve*. The second step consists of computing the optimal path(s) for the chosen Pareto optimal(s) and is denoted as the *backward solve*. In this Appendix, we outline the numerical schemes needed to solve the PDE, Pareto solutions, and ODEs involved in these steps.

A.1. Forward solve

The full PDE for energy–time optimal path planning given in Eq. (26) is of the form,

$$\frac{\partial \phi}{\partial t} + H\left(\frac{\partial \phi}{\partial \boldsymbol{x}^{\boldsymbol{a}}}, \boldsymbol{x}^{\boldsymbol{a}}, t\right) = 0. \tag{A.1}$$

The PDEs in the form of Eq. (A.1) are known as Hamilton–Jacobi equations [83–85]. H is referred to as the Hamiltonian function which, in general, depends on the augmented gradient $\frac{\partial \phi}{\partial \boldsymbol{x}^{\boldsymbol{a}}} \in \mathbb{R}^{d+1}$ and space $\boldsymbol{x}^{\boldsymbol{a}} \in \mathbb{R}^{d+1}$, and time. Presently, for Eq. (26), the Hamiltonian is:

$$H\left(\frac{\partial \phi}{\partial \boldsymbol{x}^{\boldsymbol{a}}}, \boldsymbol{x}^{\boldsymbol{a}}, t\right) = F^*(\boldsymbol{x}, e, t) \left\| \frac{\partial \phi}{\partial \boldsymbol{x}} \right\| + \boldsymbol{V}(\boldsymbol{x}, t)^T \cdot \frac{\partial \phi}{\partial \boldsymbol{x}} + \left[\dot{Q}(\boldsymbol{x}, t) - k \cdot [F^*(\boldsymbol{x}, e, t)]^n \right] \cdot \frac{\partial \phi}{\partial e}. \tag{A.2}$$

Due to their broad applicability, Hamilton–Jacobi Eqs. (A.1) have been extensively studied and the existence, uniqueness and properties of their viscosity solutions have been rigorously analyzed [83,85]. For further details, we refer to these references.

Several options exist for numerically discretizing and computing a viscosity solution to such Hamilton–Jacobi equations, ranging from Finite Volume methods to high-order discontinuous Galerkin methods [86,87], and especially level set methods [7,88]. In this work, high-order finite difference methods have been used to resolve solutions on structured, uniform, rectangular meshes.

A popular scheme for numerically computing viscosity solutions for Hamilton–Jacobi equations is the Local Lax–Friedrichs (LLF) scheme [84], and this is the scheme we use in this work. This falls under the class of what are known as monotone schemes. For Eq. (A.1), the LLF scheme results in the following semi-discretized (i.e. discretizing only in space) equation

$$\frac{\partial \phi_i}{\partial t} + \hat{H}^{LLF}\left(\left[\frac{\partial \phi}{\partial \boldsymbol{x}^{\boldsymbol{a}}}\right]_i^+, \left[\frac{\partial \phi}{\partial \boldsymbol{x}^{\boldsymbol{a}}}\right]_i^-, \boldsymbol{x}_i^{\boldsymbol{a}}, t\right) = 0, \tag{A.3}$$

where $\hat{H}^{LLF}$ is a numerical approximation of the Hamiltonian – called a numerical Hamiltonian – and ϕ_i is the value of the field $\phi(\boldsymbol{x}, t)$ at a given node, at position $\boldsymbol{x}_i$, in the finite difference mesh. Additionally, $[\frac{\partial \phi}{\partial \boldsymbol{x}^{\boldsymbol{a}}}]_i^+ \in \mathbb{R}^{d+1}$ and $[\frac{\partial \phi}{\partial \boldsymbol{x}^{\boldsymbol{a}}}]_i^- \in \mathbb{R}^{d+1}$ are one-sided discrete approximations to the spatial gradient at the node. In the LLF scheme, this numerical Hamiltonian is further given as

$$\begin{aligned}\hat{H}^{LLF}\left(\left[\frac{\partial \phi}{\partial \boldsymbol{x}^{\boldsymbol{a}}}\right]_i^+, \left[\frac{\partial \phi}{\partial \boldsymbol{x}^{\boldsymbol{a}}}\right]_i^-, \boldsymbol{x}_i^{\boldsymbol{a}}, t\right) = H\left(\frac{1}{2}\cdot\left(\left[\frac{\partial \phi}{\partial \boldsymbol{x}^{\boldsymbol{a}}}\right]_i^+ + \left[\frac{\partial \phi}{\partial \boldsymbol{x}^{\boldsymbol{a}}}\right]_i^-\right), \boldsymbol{x}_i^{\boldsymbol{a}}, t\right) \\ - \sum_{k=1}^{d+1} \frac{\alpha_k}{2} \cdot \left(\left[\frac{\partial \phi}{\partial \boldsymbol{x}^{\boldsymbol{a}}}\right]_{i,k}^+ - \left[\frac{\partial \phi}{\partial \boldsymbol{x}^{\boldsymbol{a}}}\right]_{i,k}^-\right),\end{aligned} \tag{A.4}$$

where $[\frac{\partial \phi}{\partial \boldsymbol{x}^{\boldsymbol{a}}}]_{i,k}^+$ and $[\frac{\partial \phi}{\partial \boldsymbol{x}^{\boldsymbol{a}}}]_{i,k}^-$ are the kth components of the one-sided spatial gradient approximations. The parameters α_k are dissipation coefficients that control the amount of numerical viscosity and are given as

$$\alpha_k = \max_{\boldsymbol{p} \in I} |H_k(\boldsymbol{p}, \boldsymbol{x}_i, t)|, \tag{A.5}$$

where H_k is the partial derivative of the Hamiltonian with respect to the kth component of the gradient $\frac{\partial \phi}{\partial \boldsymbol{x}^{\boldsymbol{a}}}$, $\boldsymbol{p}$ is a gradient argument and the domain I to perform the maximization over is dictated by the values of the one-sided approximations to the gradient and, in the LLF scheme, this domain varies from grid point to grid point. For further details on the LLF scheme, we refer to [83,84]. Finally, with the spatial discretization specified, all that remains is to address the temporal discretization in Eq. (A.3), for which second order total variation diminishing (TVD) Runge–Kutta (RK) schemes are an adequate choice.

For the energy–time Hamilton–Jacobi PDE (26), a closed form solution for the maximization of the partial derivatives of the Hamiltonian is not available for computing the dissipation coefficients of Eq. (A.5). Presently, a simple grid search over the interval I is used to solve the maximization problem. This has been quite effective for the applications shown in Section 4, but more advanced options are possible. Of course, to avoid numerical instabilities, the artificial dissipation could be increased with the drawback of obtaining a correspondingly more dissipative, albeit stable, numerical solution.

The following are additional details regarding the numerical discretization for the forward solve:

- For boundaries of the physical domain open to inlets/outlets or side walls, zero normal gradient (Neumann) boundary conditions were used. For further information, we refer to [7].
- Islands, obstacles and forbidden regions in the physical space are treated by following the masking procedure outlined in [7,68].
- For boundaries along the energy domain, zero Neumann boundary conditions were used.
- When numerically solving the energy–time Hamilton–Jacobi PDE to propagate the reachability front, high gradients can result in unresolved numerical solutions. To address this, a reinitialization procedure can be used every few time steps [83].

While the above LLF scheme was used to generate all results presented in this work, we also derived an efficient Global Lax–Friedrichs scheme that, although slightly more dissipative, is less computationally intensive. This scheme has been used for computing energy–time optimal paths in realistic environments using forecasts from our MIT-MSEAS modeling system [64,65] and its details are discussed further in [89].

A.2. Pareto front

Once the reachable set is evolved, the next step is to numerically compute the Pareto optimal solutions defined by Eq. (28) in Section 3.2.2. Here, we explain how to compute the Pareto front and these solutions. We start with the set of feasible states at the destination given by Eq. (27), restated here for convenience:

$$\mathcal{F}_{\boldsymbol{x}_f} = \{(e,t) \mid \phi(\boldsymbol{x}_f, e, t) \leq 0\} \ .$$

This set is obtained by keeping a record in memory of the values of (e,t) for which the implicit function is non-positive at the target point $\boldsymbol{x}_f$, as ϕ is evolved during the forward solve. Let $t_i,\ i = 1,2,\ldots,N_t$ be the discrete times considered when numerically evolving the implicit function and when this set of feasible states is saved. The Pareto optimal solutions are then computed as follows. First, we preform a maximization at every discrete time t_i to obtain $e_{max,i} = \max\{e \mid \phi(\boldsymbol{x}_f, e, t_i) \leq 0\}$ from the saved set of feasible states at these times. Each resulting $e_{max,i}$ is the maximum available energy for a vehicle that reaches the destination $\boldsymbol{x}_f$ at time t_i. The set of solutions $\tilde{\mathcal{P}} = \{(e_{max,i}, t_i) \mid 1 \leq i \leq N_t\}$ forms the envelope of highest "vehicle energy at destination" solutions at these discrete times t_i. This set is processed to compute the full Pareto front, $\mathcal{P}$, by eliminating all candidate solutions from $\tilde{\mathcal{P}}$ which are not Pareto optimal:

$$\mathcal{P} = \{(e_i,t_i) \in \tilde{\mathcal{P}} \mid \{(e_j,t_j) \in \tilde{\mathcal{P}} \mid t_j < t_i \text{ and } e_j > e_i\} = \emptyset\} \ .$$

In other words, a candidate solution $(e_i,t_i) \in \tilde{\mathcal{P}}$ is not Pareto optimal if we can find a solution at an earlier time with a higher energy, i.e. there is at least a path for the vehicle to reach the end faster and with more energy. Eliminating all these sub-optimal solutions, we obtain the set of Pareto optimal solutions $\mathcal{P}$.

A.3. Backward solve

Once the forward solve has generated the Pareto front, the backtracking Eq. (29) is integrated to compute the optimal paths for the selected Pareto optimal solution(s). This is a system of ODEs that is discretized and solved using standard explicit or implicit schemes, as outlined in [7].

In this work, an implicit first order time integration scheme was used to backtrack all optimal paths. Denoting the augmented state of the vehicle at time t as $(\boldsymbol{X}_{\boldsymbol{p}}^{\boldsymbol{a},*})_t$, the discretized form of Eq. (29) is,

$$\frac{(\boldsymbol{X}_{\boldsymbol{p}}^{\boldsymbol{a},*})_{t+\Delta t} - (\boldsymbol{X}_{\boldsymbol{p}}^{\boldsymbol{a},*})_t}{\Delta t} = -\boldsymbol{U}_*^{\boldsymbol{a}}((\boldsymbol{X}_{\boldsymbol{p}}^{\boldsymbol{a},*})_t, t) - \boldsymbol{V}^{\boldsymbol{a}}((\boldsymbol{X}_{\boldsymbol{p}}^{\boldsymbol{a},*})_t, t). \tag{A.6}$$

It is important to note that Eq. (A.6) is indeed implicit, as the backtracking equation is solved *backward* in time starting from the final state $(\boldsymbol{X}_{\boldsymbol{p}}^{\boldsymbol{a},*})_{t_f}$ at the final time t_f. Therefore, at each time step, $(\boldsymbol{X}_{\boldsymbol{p}}^{\boldsymbol{a},*})_{t+\Delta t}$ is known whereas $(\boldsymbol{X}_{\boldsymbol{p}}^{\boldsymbol{a},*})_t$ is the unknown. Solving for $(\boldsymbol{X}_{\boldsymbol{p}}^{\boldsymbol{a},*})_t$ requires the solution of a system of nonlinear equations for which a fixed point scheme can be used. For the benefits of using an implicit backtracking scheme, we refer to [69].

Appendix B. Semi analytical solution for the highway case

The goal is to compute a semi-analytical solution for the Crossing of a Jet Flow (Section 4.1), so as to validate our theory and numerical results. All variables used in this Appendix are defined in Fig. 3.

Consider an initial spherical reachability front centered at (x_c, y_c, e_c) in the augmented state space and with initial radius r_0. Our aim, recall, is to determine Pareto optimal paths originating from anywhere in this reachable set to the destination that minimize travel time and energy usage. Intuitively, it is clear that any such Pareto optimal path must originate from a state on the boundary of the reachable set — the reachability front. The unknown start point of the path from the spherical front can be parametrized using two degrees of freedom as:

$$\begin{aligned} x_i(\alpha, \beta) &= x_c + r_0\ sin(\beta)\ cos(\alpha) \\ y_i(\alpha, \beta) &= y_c + r_0\ sin(\beta)\ sin(\alpha) \\ e_i(\alpha, \beta) &= e_c + r_0\ cos(\beta). \end{aligned} \tag{B.1}$$

The variables α and β correspond to the angular positions of the start point on the front, where α denotes the polar angle and β the azimuthal angle as defined in the standard spherical coordinate system. Consider now the motion of the vehicle through the three main segments of the domain — before the jet, within the jet, and after the jet. Given the constant environment faced by the vehicle in each of these segments, the optimal speed of the vehicle will be constant within them. The net vertical distance traveled by the vehicle in the first segment before the jet is given as $\Delta\tilde{y}_1 = \Delta y_1 - r_0\ sin(\beta)\ sin(\alpha)$. The net horizontal distance that the vehicle must travel to reach the target is $\Delta x = \Delta x_0 - r_0\ sin(\beta)\ cos(\alpha)$. The time taken by the vehicle in each segment is given as:

$$\begin{aligned} T_1(F_1, \theta_1, \alpha, \beta) &= \frac{\Delta\tilde{y}_1}{F_1 cos(\theta_1)} = \frac{\Delta y_1 - r_0\ sin(\alpha)\ sin(\beta)}{F_1\ cos(\theta_1)} \\ T_2(F_2, \theta_2) &= \frac{\Delta y_2}{F_2\ cos(\theta_2)} \\ T_3(F_3, \theta_3) &= \frac{\Delta y_3}{F_3\ cos(\theta_3)}. \end{aligned} \tag{B.2}$$

The total time taken to travel the required vertical distance is then given as $T(\boldsymbol{\theta}, \boldsymbol{F}, \alpha, \beta) = T_1 + T_2 + T_3$, where $\boldsymbol{F} = [F_1, F_2, F_3]^T$ and $\boldsymbol{\theta} = [\theta_1, \theta_2, \theta_3]^T$ correspond to the speed and headings in each segment (refer to Fig. 3). Since the time taken to traverse the vertical and horizontal distances to the target are the same, we have the following constraint on the horizontal distance that must be traveled by the vehicle:

$$\Delta x_0 - r_0\ sin(\beta)\ cos(\alpha) - \Delta x(\boldsymbol{\theta}, \boldsymbol{F}, \alpha, \beta) = 0 \tag{B.3}$$

where $\Delta x(\boldsymbol{\theta}, \boldsymbol{F}, \alpha, \beta) = F_1\ T_1\ sin(\theta_1) + T_2\ [F_2 sin(\theta_2) + V] + F_3\ T_3\ sin(\theta_3)$ corresponds to the horizontal displacement of the vehicle, given a set of headings and speeds chosen. Finally, the energy used by the vehicle is given as $e_{used}(\boldsymbol{\theta}, \boldsymbol{F}, \alpha, \beta) = k\,T_1 F_1^3 + k\,T_2 F_2^3 + k\,T_3 F_3^3$, resulting in the energy remaining in the vehicle at the destination to be:

$$e_{dest}(\boldsymbol{\theta}, \boldsymbol{F}, \alpha, \beta) = e_i(\alpha, \beta) - e_{used}(\boldsymbol{\theta}, \boldsymbol{F}, \alpha, \beta). \tag{B.4}$$

With the travel time and energy at destination defined, we can finally define the optimization problem to obtain the semi-analytical solutions. The Pareto front of the multi-objective optimization problem is built by solving a series of constrained optimization problems to minimize the travel time:

$$\begin{aligned} \underset{\boldsymbol{F}, \boldsymbol{\theta}, \alpha, \beta}{\text{minimize}} \quad & T(\boldsymbol{\theta}, \boldsymbol{F}, \alpha, \beta) \\ \text{subject to} \quad & e_{dest}(\boldsymbol{\theta}, \boldsymbol{F}, \alpha, \beta) \geq e_f \\ & \Delta x_0 - r_0\ sin(\beta)\ cos(\alpha) - \Delta x(\boldsymbol{\theta}, \boldsymbol{F}, \alpha, \beta) = 0. \end{aligned} \tag{B.5}$$

For each E_{min} value on the Pareto front, the corresponding minimal arrival time is computed by solving Eq. (B.5).

References

[1] G. Griffiths, Technology and Applications of Autonomous Underwater Vehicles, Vol. 2, CRC Press, 2002.

[2] O. Schofield, S. Glenn, J. Orcutt, M. Arrott, M. Meisinger, A. Gangopadhyay, W. Brown, R. Signell, M. Moline, Y. Chao, S. Chien, D. Thompson, A. Balasuriya, P.F.J. Lermusiaux, M. Oliver, Automated sensor networks to advance ocean science, Eos Trans. AGU 91 (39) (2010) 345–346.
[3] D. Floreano, R.J. Wood, Science, technology and the future of small autonomous drones, Nature 521 (7553) (2015) 460–466.
[4] S.A. Bagloee, M. Tavana, M. Asadi, T. Oliver, Autonomous vehicles: challenges, opportunities, and future implications for transportation policies, J. Mod. Transp. 24 (4) (2016) 284–303.
[5] P.F.J. Lermusiaux, D.N. Subramani, J. Lin, C.S. Kulkarni, A. Gupta, A. Dutt, T. Lolla, P.J. Haley Jr., W.H. Ali, C. Mirabito, S. Jana, A future for intelligent autonomous ocean observing systems, J. Mar. Res. 75 (6) (2017) 765–813, The Sea. Volume 17, The Science of Ocean Prediction, Part 2.
[6] R.R. Murphy, Introduction to AI Robotics, MIT Press, 2019.
[7] T. Lolla, P.F.J. Lermusiaux, M.P. Ueckermann, P.J. Haley Jr., Time-optimal path planning in dynamic flows using level set equations: Theory and schemes, Ocean Dyn. 64 (10) (2014) 1373–1397.
[8] S.V.T. Lolla, Path Planning and Adaptive Sampling in the Coastal Ocean (Ph.D. thesis), Massachusetts Institute of Technology, Department of Mechanical Engineering, Cambridge, Massachusetts, 2016.
[9] D.N. Subramani, P.F.J. Lermusiaux, Energy-optimal path planning by stochastic dynamically orthogonal level-set optimization, Ocean Model. 100 (2016) 57–77.
[10] J.G. Bellingham, K. Rajan, Robotics in remote and hostile environments, Science 318 (5853) (2007) 1098–1102.
[11] T.H. Karakoc, C.O. Colpan, O. Altuntas, Y. Sohret, Sustainable Aviation, Springer, 2019.
[12] Z. Wan, M. Zhu, S. Chen, D. Sperling, Pollution: Three steps to a green shipping industry, Nature 530 (7590) (2016) 275–277.
[13] D.C. Webb, P.J. Simonetti, C.P. Jones, SLOCUM: An underwater glider propelled by environmental energy, IEEE J. Ocean. Eng. 26 (4) (2001) 447–452.
[14] G. Reader, J. Potter, J. Hawley, The evolution of AUV power systems, in: OCEANS'02 MTS/IEEE, Vol.1, IEEE, 2002, pp. 191–198.
[15] J.P. Panda, A. Mitra, H.V. Warrior, A review on the hydrodynamic characteristics of autonomous underwater vehicles, Proc. Inst. Mech. Eng. 235 (1) (2021) 15–29.
[16] J.G. Bellingham, Y. Zhang, J.E. Kerwin, J. Erikson, B. Hobson, B. Kieft, M. Godin, R. McEwen, T. Hoover, J. Paul, A. Hamilton, J. Franklin, A. Banka, Efficient propulsion for the Tethys long-range autonomous underwater vehicle, in: 2010 IEEE/OES Autonomous Underwater Vehicles, 2010, pp. 1–7.
[17] D.R. Blidberg, M.D. Ageev, Solar powered autonomous underwater vehicles, in: G. Griffiths (Ed.), Technology and Applications of Autonomous Underwater Vehicles, Taylor & Francis, 2002, pp. 59–76, URL https://eprints.soton.ac.uk/22121/.
[18] M.D. Ageev, An analysis of long-range AUV, powered by solar energy, in: Challenges of Our Changing Global Environment. Conference Proceedings. OCEANS'95 MTS/IEEE, Vol. 2, IEEE, 1995, pp. 809–813.
[19] M.D. Ageev, Solar and wave powered AUV concept, in: Proceedings of the 2000 International Symposium on Underwater Technology (Cat. No. 00EX418), IEEE, 2000, pp. 136–139.
[20] J. Jalbert, J. Baker, J. Duchesney, P. Pietryka, W. Dalton, D. Blidberg, S. Chappell, R. Nitzel, K. Holappa, A solar-powered autonomous underwater vehicle, in: Oceans 2003. Celebrating the Past... Teaming Toward the Future (IEEE Cat. No. 03CH37492), Vol. 2, IEEE, 2003, pp. 1132–1140.
[21] D.M. Crimmins, C.T. Patty, M.A. Beliard, J. Baker, J.C. Jalbert, R.J. Komerska, S.G. Chappell, D.R. Blidberg, Long-endurance test results of the solar-powered AUV system, in: OCEANS 2006, IEEE, 2006, pp. 1–5.
[22] Øistein Hasvold, N.J. Størkersen, S. Forseth, T. Lian, Power sources for autonomous underwater vehicles, J. Power Sources 162 (2) (2006) 935–942, Special issue including selected papers from the International Power Sources Symposium 2005 together with regular papers, URL http://www.sciencedirect.com/science/article/pii/S0378775305008608.
[23] I. Vasilescu, C. Detweiler, M. Doniec, D. Gurdan, S. Sosnowski, J. Stumpf, D. Rus, AMOUR v: A hovering energy efficient underwater robot capable of dynamic payloads, Int. J. Robot. Res. 29 (5) (2010) 547–570, http://dx.doi.org/10.1177/0278364909358275.
[24] S.A. Sharkh, G. Griffiths, A. Webb, Power sources for unmanned underwater vehicles, in: G. Griffiths (Ed.), Technology and Applications of Autonomous Underwater Vehicles, Taylor & Francis, 2002, pp. 19–35, URL https://eprints.soton.ac.uk/22121/.
[25] P. Godart, J. Fischman, D. Hart, Kilowatt-scale fuel cell systems powered by recycled aluminum, J. Electrochem. Energy Convers. Storage 18 (1) (2021).
[26] N.B. Pulsone, D.P. Hart, A.M. Siegel, J.R. Edwards, K.E. Railey, Aluminum-water energy system for autonomous undersea vehicles, Linc. Lab. J. 22 (2) (2017) 79–90.
[27] L.M. Ware, Design of control for efficiency of AUV power systems; Design of control for efficiency of Autonomous Underwater Vehicle power systems (Ph.D. thesis), MIT, 2012.
[28] J.-C. Latombe, Robot Motion Planning, Vol. 124, Springer Science & Business Media, 2012.
[29] J.J. Leonard, A. Bahr, Autonomous underwater vehicle navigation, in: Springer Handbook of Ocean Engineering, Springer International Publishing, Cham, 2016, pp. 341–358, http://dx.doi.org/10.1007/978-3-319-16649-0_14.
[30] H. Schmidt, J.G. Bellingham, M. Johnson, D. Herold, D.M. Farmer, R. Pawlowicz, Real-time frontal mapping with AUVs in a coastal environment, in: OCEANS 96 MTS/IEEE Conference Proceedings. The Coastal Ocean-Prospects for the 21st Century, Vol. 3, IEEE, 1996, pp. 1094–1098.
[31] D.L. Rudnick, R.E. Davis, C.C. Eriksen, D.M. Fratantoni, M.J. Perry, Underwater gliders for ocean research, Mar. Technol. Soc. J. 38 (2) (2004) 73–84.
[32] A. Chakrabarty, J.W. Langelaan, Energy-based long-range path planning for soaring-capable unmanned aerial vehicles, J. Guid. Control Dyn. 34 (4) (2011) 1002–1015.
[33] M.N. Boukoberine, R. Khattar, M. Benbouzid, N. Moubayed, Drone resilient control against actuator failures and wind gusts, in: 2022 IEEE Transportation Electrification Conference and Expo, ITEC, 2022, pp. 313–318.

[34] S. Bansal, M. Chen, S. Herbert, C.J. Tomlin, Hamilton-Jacobi reachability: A brief overview and recent advances, in: 2017 IEEE 56th Annual Conference on Decision and Control, CDC, IEEE, 2017, pp. 2242–2253.
[35] T. Lolla, P.F.J. Lermusiaux, A Forward Reachability Equation for Minimum-Time Path Planning in Strong Dynamic Flows, MSEAS Report 27, Department of Mechanical Engineering, Massachusetts Institute of Technology, Cambridge, MA, USA, 2017.
[36] T. Lolla, M.P. Ueckermann, K. Yiğit, P.J. Haley Jr., P.F.J. Lermusiaux, Path planning in time dependent flow fields using level set methods, in: IEEE International Conference on Robotics and Automation, ICRA, 14–18 May 2012, 2012, pp. 166–173.
[37] K.P. Carroll, S.R. McClaran, E.L. Nelson, D.M. Barnett, D.K. Friesen, G.N. William, AUV path planning: an A* approach to path planning with consideration of variable vehicle speeds and multiple, overlapping, time-dependent exclusion zones, in: Proceedings of the 1992 Symposium on Autonomous Underwater Vehicle Technology, IEEE, 1992, pp. 79–84.
[38] B. Garau, A. Alvarez, G. Oliver, Path planning of autonomous underwater vehicles in current fields with complex spatial variability: an A* approach, in: Proceedings of the 2005 IEEE International Conference on Robotics and Automation, IEEE, 2005, pp. 194–198.
[39] D. Kularatne, S. Bhattacharya, M.A. Hsieh, Time and energy optimal path planning in general flows, in: Robotics: Science and Systems, 2016.
[40] V.T. Huynh, M. Dunbabin, R.N. Smith, Predictive motion planning for AUVs subject to strong time-varying currents and forecasting uncertainties, in: 2015 IEEE International Conference on Robotics and Automation, ICRA, IEEE, 2015, pp. 1144–1151.
[41] T.-B. Koay, M. Chitre, Energy-efficient path planning for fully propelled AUVs in congested coastal waters, in: 2013 MTS/IEEE OCEANS-Bergen, IEEE, 2013, pp. 1–9.
[42] D. Rao, S.B. Williams, Large-scale path planning for underwater gliders in ocean currents, in: Australasian Conference on Robotics and Automation, ACRA, 2009, pp. 2–4.
[43] Z. Zeng, K. Sammut, L. Lian, F. He, A. Lammas, Y. Tang, A comparison of optimization techniques for AUV path planning in environments with ocean currents, Robot. Auton. Syst. 82 (2016) 61–72.
[44] A. Alvarez, A. Caiti, R. Onken, Evolutionary path planning for autonomous underwater vehicles in a variable ocean, IEEE J. Ocean. Eng. 29 (2) (2004) 418–429.
[45] J. Cao, J. Cao, Z. Zeng, L. Lian, Optimal path planning of underwater glider in 3D dubins motion with minimal energy consumption, in: OCEANS 2016-Shanghai, IEEE, 2016, pp. 1–7.
[46] Y. Huang, H. Wang, P. Yao, Energy-optimal path planning for solar-powered UAV with tracking moving ground target, Aerosp. Sci. Technol. 53 (2016) 241–251.
[47] D. Kruger, R. Stolkin, A. Blum, J. Briganti, Optimal AUV path planning for extended missions in complex, fast-flowing estuarine environments, in: Proceedings 2007 IEEE International Conference on Robotics and Automation, IEEE, 2007, pp. 4265–4270.
[48] J. Witt, M. Dunbabin, Go with the flow: Optimal AUV path planning in coastal environments, in: Australian Conference on Robotics and Automation, Vol. 2008, No. 2, 2008.
[49] D.N. Subramani, T. Lolla, P.J. Haley Jr., P.F.J. Lermusiaux, A stochastic optimization method for energy-based path planning, in: S. Ravela, A. Sandu (Eds.), DyDESS 2014, in: LNCS, vol. 8964, Springer, 2015, pp. 1–12.
[50] G. Mannarini, D.N. Subramani, P.F.J. Lermusiaux, N. Pinardi, Graph-search and differential equations for time-optimal vessel route planning in dynamic ocean waves, IEEE Trans. Intell. Transp. Syst. 21 (6) (2020) 1–13.
[51] M. Ehrgott, Multiobjective optimization, AI Mag. 29 (4) (2008) 47.
[52] S.M. LaValle, S.A. Hutchinson, Optimal motion planning for multiple robots having independent goals, IEEE Trans. Robot. Autom. 14 (6) (1998) 912–925.
[53] K. Miettinen, Nonlinear Multiobjective Optimization, in: International Series in Operations Research & Management Science, Springer US, 1999, URL https://books.google.com/books?id=ha_zLdNtXSMC.
[54] F.M. White, Fluid Mechanics, seventh ed., Tata McGraw-Hill Education, 1979.
[55] G. Elert, Aerodynamic drag, in: The Physics Hypertextbook, hypertextbook, 1998, URL https://physics.info/drag/.
[56] D.N. Subramani, Energy Optimal Path Planning Using Stochastic Dynamically Orthogonal Level Set Equations (Master's thesis), Massachusetts Institute of Technology, Department of Mechanical Engineering, Cambridge, Massachusetts, 2014.
[57] T. Lolla, P.J. Haley Jr., P.F.J. Lermusiaux, Time-optimal path planning in dynamic flows using level set equations: Realistic applications, Ocean Dyn. 64 (10) (2014) 1399–1417.
[58] D.N. Subramani, P.F.J. Lermusiaux, P.J. Haley Jr., C. Mirabito, S. Jana, C.S. Kulkarni, A. Girard, D. Wickman, J. Edwards, J. Smith, Time-optimal path planning: Real-time sea exercises, in: Oceans '17 MTS/IEEE Conference, Aberdeen, 2017.
[59] P.F.J. Lermusiaux, P.J. Haley Jr., S. Jana, A. Gupta, C.S. Kulkarni, C. Mirabito, W.H. Ali, D.N. Subramani, A. Dutt, J. Lin, A. Shcherbina, C. Lee, A. Gangopadhyay, Optimal planning and sampling predictions for autonomous and Lagrangian platforms and sensors in the Northern Arabian Sea, Oceanography 30 (2) (2017) 172–185, Special issue on Autonomous and Lagrangian Platforms and Sensors (ALPS).
[60] L.R. Centurioni, et al., Northern Arabian Sea circulation-autonomous research (NASCar): A research initiative based on autonomous sensors, Oceanography 30 (2) (2017) 74–87, Special issue on Autonomous and Lagrangian Platforms and Sensors (ALPS).
[61] R.J. DiPerna, P.-L. Lions, Ordinary differential equations, transport theory and Sobolev spaces, Invent. Math. 98 (3) (1989) 511–547.
[62] L. Ambrosio, Transport equation and Cauchy problem for non-smooth vector fields, in: Calculus of Variations and Nonlinear Partial Differential Equations, Springer, 2008, pp. 1–41.
[63] M.P. Ueckermann, P.F.J. Lermusiaux, 2.29 Finite Volume MATLAB Framework Documentation, MSEAS Report 14, Department of Mechanical Engineering, Massachusetts Institute of Technology, Cambridge, MA, 2012, URL http://mseas.mit.edu/?p=2567.
[64] P.J. Haley Jr., P.F.J. Lermusiaux, Multiscale two-way embedding schemes for free-surface primitive equations in the "Multidisciplinary simulation, estimation and assimilation system", Ocean Dyn. 60 (6) (2010) 1497–1537.
[65] P.J. Haley Jr., A. Agarwal, P.F.J. Lermusiaux, Optimizing velocities and transports for complex coastal regions and archipelagos, Ocean Model. 89 (2015) 1–28.

[66] D.N. Subramani, P.J. Haley Jr., P.F.J. Lermusiaux, Energy-optimal path planning in the coastal ocean, J. Geophys. Res.: Oceans 122 (2017) 3981–4003.
[67] M. Aguiar, J.B. de Sousa, J.M. Dias, J.E. da Silva, R. Mendes, A.S. Ribeiro, Optimizing autonomous underwater vehicle routes with the aid of high resolution ocean models, in: OCEANS 2019 MTS/IEEE SEATTLE, IEEE, 2019, pp. 1–7.
[68] T. Lolla, P.J. Haley Jr., P.F.J. Lermusiaux, Path planning in multiscale ocean flows: Coordination and dynamic obstacles, Ocean Model. 94 (2015) 46–66.
[69] C.S. Kulkarni, P.F.J. Lermusiaux, Three-dimensional time-optimal path planning in the ocean, Ocean Model. 152 (2020).
[70] L. Lebreton, B. Slat, F. Ferrari, B. Sainte-Rose, J. Aitken, R. Marthouse, S. Hajbane, S. Cunsolo, A. Schwarz, A. Levivier, et al., Evidence that the Great Pacific Garbage Patch is rapidly accumulating plastic, Sci. Rep. 8 (1) (2018) 1–15.
[71] P.F.J. Lermusiaux, M. Doshi, C.S. Kulkarni, A. Gupta, P.J. Haley Jr., C. Mirabito, F. Trotta, S.J. Levang, G.R. Flierl, J. Marshall, T. Peacock, C. Noble, Plastic pollution in the coastal oceans: Characterization and modeling, in: OCEANS 2019 MTS/IEEE SEATTLE, IEEE, Seattle, 2019, pp. 1–10.
[72] M.S. Bhabra, M. Doshi, B.C. Koenig, P.J. Haley Jr., C. Mirabito, P.F.J. Lermusiaux, C.A. Goudey, J. Curcio, D. Manganelli, H. Goudey, Optimal harvesting with autonomous tow vessels for offshore macroalgae farming, in: OCEANS 2020 IEEE/MTS, IEEE, 2020, pp. 1–10.
[73] D.N. Subramani, Q.J. Wei, P.F.J. Lermusiaux, Stochastic time-optimal path-planning in uncertain, strong, and dynamic flows, Comput. Methods Appl. Mech. Engrg. 333 (2018) 218–237.
[74] D.N. Subramani, P.F.J. Lermusiaux, Risk-optimal path planning in stochastic dynamic environments, Comput. Methods Appl. Mech. Engrg. 353 (2019) 391–415.
[75] P.F.J. Lermusiaux, T. Lolla, P.J. Haley Jr., K. Yigit, M.P. Ueckermann, T. Sondergaard, W.G. Leslie, Science of autonomy: Time-optimal path planning and adaptive sampling for swarms of ocean vehicles, in: T. Curtin (Ed.), Springer Handbook of Ocean Engineering: Autonomous Ocean Vehicles, Subsystems and Control, Springer, 2016, pp. 481–498.
[76] P.F.J. Lermusiaux, P.J. Haley Jr., N.K. Yilmaz, Environmental prediction, path planning and adaptive sampling: Sensing and modeling for efficient ocean monitoring, management and pollution control, Sea Technol. 48 (9) (2007) 35–38.
[77] P.F.J. Lermusiaux, Adaptive modeling, adaptive data assimilation and adaptive sampling, Physica D 230 (1) (2007) 172–196.
[78] K. Rajan, F. Aguado, P. Lermusiaux, J.B. de Sousa, A. Subramaniam, J. Tintore, METEOR: A Mobile (Portable) ocEan roboTic ObsErvatORy, Mar. Technol. Soc. J. 55 (3) (2021) 74–75.
[79] J. Ding, J. Sprinkle, S.S. Sastry, C.J. Tomlin, Reachability calculations for automated aerial refueling, in: 2008 47th IEEE Conference on Decision and Control, 2008, pp. 3706–3712.
[80] J.H. Gillula, G.M. Hoffmann, H. Huang, M.P. Vitus, C.J. Tomlin, Applications of hybrid reachability analysis to robotic aerial vehicles, Int. J. Robot. Res. 30 (3) (2011) 335–354, http://dx.doi.org/10.1177/0278364910387173.
[81] W. Sun, P. Tsiotras, T. Lolla, D.N. Subramani, P.F.J. Lermusiaux, Multiple-pursuer-one-evader pursuit evasion game in dynamic flow fields, J. Guid. Control Dyn. 40 (7) (2017).
[82] S.S. Joshi, S. Hutchinson, P. Tsiotras, TIE: Time-informed exploration for robot motion planning, IEEE Robot. Autom. Lett. 6 (2) (2021) 3585–3591.
[83] S. Osher, R.P. Fedkiw, Level Set Methods and Dynamic Implicit Surfaces, Vol. 1, Springer New York, 2005.
[84] C.-W. Shu, High order numerical methods for time dependent Hamilton–Jacobi equations, in: Mathematics and Computation in Imaging Science and Information Processing, World Scientific, 2007, pp. 47–91.
[85] L. Evans, Partial Differential Equations, in: Graduate Studies in Mathematics, American Mathematical Society, 2010, URL https://books.google.ca/books?id=Xnu0o_EJrCQC.
[86] H. Lomax, T.H. Pulliam, D.W. Zingg, Fundamentals of Computational Fluid Dynamics, Springer Science & Business Media, 2013.
[87] J.S. Hesthaven, T. Warburton, Nodal Discontinuous Galerkin Methods: Algorithms, Analysis, and Applications, Springer Science & Business Media, 2007.
[88] I.M. Mitchell, The flexible, extensible and efficient toolbox of level set methods, J. Sci. Comput. 35 (2) (2008) 300–329.
[89] M.M. Doshi, M.S. Bhabra, P.F.J. Lermusiaux, Energy-time optimal path planning in dynamic flows: Realistic applications, 2023, in preparation.